



# Microfluidic Femtoliter Droplets Exposed to Laser Potentials

Master Thesis

by

Sebastian Horstmann

September 2017

Faculty of Mathematics and Natural Sciences

---

Supervision:  
Univ.-Prof. Dr. S. Egelhaaf  
Christoph Zunke  
Dr. Florian Platten

Examination:  
Univ.-Prof. Dr. S. Egelhaaf  
Univ.-Prof. Dr. A. Görlitz

---

# Abstract

Droplet emulsions feature a variety of advantages over generic colloidal systems. Their phase composition can be adjusted and it is possible to form them on demand. However, mesoscopic particle dispersions perform Brownian motion, and often the subject of studies is their reaction on laser potential exposure. Thus, droplets must be generated uniformly and in micrometer sizes to be sufficiently small. Soft lithography fabrication is used to build a microfluidic platform for femtoliter-volume droplet formation. Also, droplet emulsions easily break down due to free energy preferences. This issue is overcome by adding fluorosurfactant to the oil medium and achieve probe stabilities of at least a month. To manipulate emulsions with laser forces, their refractive index is being tuned by adding sucrose to the dispersed phase. It is shown that droplet emulsions present an equally well-suited model system as that of colloidal dispersions. Moreover, proof is provided that rough laser potentials induce sub-diffusion in the dynamics of dilute droplet emulsions, while cage constraints dominate for dense probes.



# Contents

<b>1</b>	<b>Introduction</b>	<b>1</b>
<b>2</b>	<b>Controlled formation of droplet emulsions</b>	<b>5</b>
2.1	Immiscible two-phase liquid systems . . . . .	6
2.2	Low Reynolds number hydrodynamics . . . . .	7
2.2.1	Laminar flow in microfluidic channels . . . . .	8
2.2.2	Hydrodynamic resistance . . . . .	9
2.2.3	Kirchhoff's law analogy . . . . .	11
2.3	Droplet microfluidics . . . . .	11
2.3.1	Flow focusing . . . . .	12
2.3.2	Capillary and Weber number . . . . .	13
2.3.3	Jetting effects . . . . .	14
<b>3</b>	<b>Construction of a microfluidic platform for femtoliter droplet generation</b>	<b>15</b>
3.1	Glass-capillary and polymer-mold devices . . . . .	16
3.2	Soft lithography chip fabrication . . . . .	17
3.2.1	Master assembly . . . . .	18
3.2.2	Replica molding . . . . .	21
3.3	Microfluidics: injection and acquisition . . . . .	24
3.3.1	Image acquisition . . . . .	25
3.3.2	Volume-driven flow . . . . .	26
3.3.3	Pressure-driven flow . . . . .	26
3.4	Miniaturization to femtoliter droplet regime . . . . .	27
3.4.1	Two-layer chip design . . . . .	28
3.4.2	High-precision chrome photomask . . . . .	30
3.4.3	Overall hydrodynamic resistance . . . . .	31

<b>4</b>	<b>Stabilization and characterization of mesoscopic droplet dispersions</b>	<b>35</b>
4.1	Composing stable micro-droplet emulsions . . . . .	36
4.1.1	Dispersed droplet phase . . . . .	36
4.1.2	Continuous carrier phase . . . . .	37
4.1.3	Gibbs free energy stabilization . . . . .	38
4.1.4	Creaming and sedimentation . . . . .	41
4.2	Colloidal systems . . . . .	42
4.2.1	Brownian motion . . . . .	43
4.2.2	Anomalous diffusion . . . . .	43
4.3	Characterization of microfluidically designed emulsions . . . . .	45
4.3.1	Polydispersity in stored probes . . . . .	45
4.3.2	Droplet and particle dynamics . . . . .	47
4.3.3	Pair-distribution in very dense configurations . . . . .	50
<b>5</b>	<b>Exposure of micro-droplets to laser potentials</b>	<b>53</b>
5.1	Forces exerted by optical tweezers . . . . .	54
5.2	Refractive index adjustment of the dispersed phase . . . . .	55
5.3	Single beam trapping of droplets in a flow . . . . .	56
5.3.1	Estimation of the trap stiffness . . . . .	58
5.4	Rough laser potentials . . . . .	59
5.4.1	Effect on dilute sucrose droplet emulsions . . . . .	59
5.4.2	Different laser powers on dense droplet emulsions . . . . .	62
<b>6</b>	<b>Conclusion and outlook</b>	<b>67</b>
	<b>Bibliography</b>	<b>71</b>

# Chapter 1

## Introduction

Microdroplets arise in a considerable variety of technologies with applications in everything from paints and coatings to foods and drugs [Philippe Poulin and Weitz, 1997]. However, a very popular and exemplary droplet-based system is milk. Being part of nearly every European's breakfast, it consists of two immiscible phases. As Fig. 1.1<sup>1</sup> shows, a two-phase system's oil and water phases do not just mix. Instead, a separation line forms which tries to minimize its interface. But, promoted by the excellent emulsifying properties of milk's casein proteins, one phase forms droplets within the other, see Fig. 1.1 b). Thus, a dispersed system like this is called an emulsion. In milk's case, oil droplets are dispersed in water. In fact, the word emulsion comes from the latin term for 'to milk'. More generally, the phase that occupies less volume shapes dispersed droplets within the continuous phase [Philipp Gruner and Baret, 2015]. But applications of droplet emulsions are even more widespread: examples are home and personal care products such as perfumes [J. Bibette et al, 1999]. Commercialized meals actively use emulsification, for example mayonnaise or salad vinaigrettes [Chappat, 1994]. However, most of the time when emulsions arise in nature they are polydisperse and not easily controlled, e.g. in cow's milk casein micelles range from 30 to 400 nanometers in size [Töpel, 2015].

Microfluidic technology has generated renewed interest in this field as multi-phase emulsions can be individually designed and accurately directed on a micrometer scale due to the device's laminar flow characteristics. Manipulation of the thermal environment, droplet composition and movement allow new experimental insights, e.g. regarding medical research in the field of drug delivery [Babak Ziaie and Siegel, 2004]. A drug containing pharmaceutical

---

<sup>1</sup>Figure by [Organic Information Services Pvt Ltd., 2017].

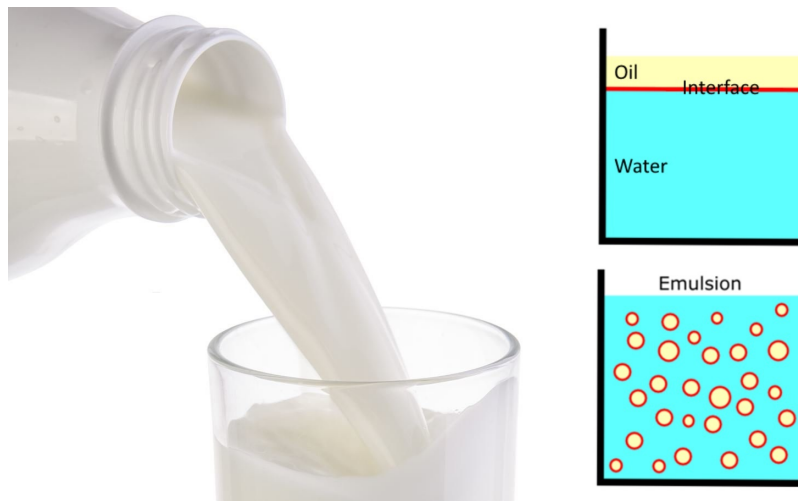


Figure 1.1: Milk is a two-phase liquid system. It features oil in water (o/w) droplets.

droplets can be injected into the bloodstream so as to enable diffusion into the target region of the human body [Ying Zhang and Leong, 2013]. Biologists are able to encapsulate single cells in droplets to identify non-functional ones or allow rapid DNA sequence analysis and genotype testing [Adam R. Abate and Weitz, 2013]. This technique is a prime example of what is considered to be a lab on a chip and promises to detect and treat cancer in the future [Jian Chen and Sun, 2012]. Chemical reactions can be performed on a tiny scale using small amounts of reagent and droplets as mini reactors. Moreover, engineers developed droplet sorting chips, as well as whole (cell-)sorting machines that are already applied in biology labs [Zhu and Nguyen, 2010]. These use passive geometrical methods [Yung-Chieh Tan and Lee, 2008] or active systems, e.g. surface acoustic waves [Thomas Franke and Wixforth, 2009]. Computer scientists are confident of being able to build the first soft matter computer using droplet microfluidics in the future [Danny Van Noort and Landweber, 2004]. Figure 1.2<sup>2</sup> shows a microfluidic chip fabricated by polymer molding. The complex structure on the device is designed to model the physiology in a human lung. This branch of microfluidics is called organ-on-a-chip and promises to decrease the need of animal testing [Eric K. Sackmann and Beebe, 2014]. In the 1990s, polymer chip production found its way into soft matter and biotechnology science laboratories. Following a paragon originally used to print electric circuit boards, engineers started to tune these patterns to fabricate fine fluid channels on substrate. Since then, accuracy and reproducibility of the so-called soft lithography technique have successively improved so that most larger science laboratories in the field are equipped with a soft materials cleanroom. Complex channel structures can

---

<sup>2</sup>Figure by [Eric K. Sackmann and Beebe, 2014].

---

now be manufactured in micrometer size resolution. These new perspectives encouraged the creativity of scientists to design channel configurations allowing to form droplets as small as ten micrometers in diameter featuring volumes close to the femtoliter regime.

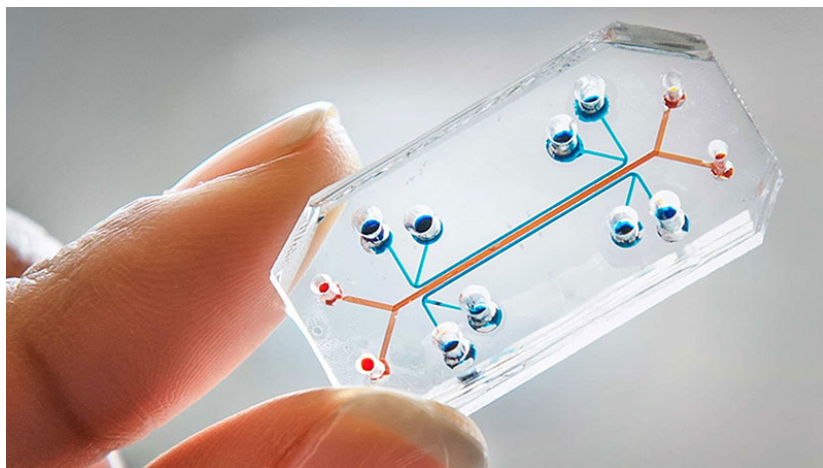


Figure 1.2: Polymer-mold microfluidic chip, often utilized in biotechnology.

In the soft matter field, colloidal suspensions serve as model systems for calculations in statistical physics [Chandrasekhar, 1943]. Externally fabricated polymer particles of sizes smaller than ten micrometers are implemented in most laboratory experiments. Colloidal particles are subject to molecular thermal dynamics and are either sterically or electrostatically shielded against neighbor interactions. Moreover, samples remain stable for months. Nonetheless, these particles have to be ordered, shipped and properties are unchangeable. This work views droplets as colloids. In fact, liquid beads can easily be tuned and self-generated in any size and whenever needed by the help of a microfluidic droplet formation chip. In the course of this thesis, it may thus be referred to droplets as bubbles (when there is gas involved), colloids or particles (when the analogy is adequate).

A key advantage of microfluidics lies in the fine control of droplets and therefore the solvent they encapsulate. Hence, a noninvasive manipulation with optical potentials is highly interesting. However, since optical forces applicable are on the order of magnitude of piconewton, the droplets inertia cannot be larger than that of colloids. Making droplets smaller than the commonly used size of about a hundred to ten micrometers, requires extended knowledge about micro-flows. Moreover, engineering work in the field of soft lithography chip production is necessary. Because channels become remarkably smaller, the pressure resistance of the chip polymer must be pushed to its maximum limit. The typically lower stability of emulsions compared to polymer suspensions must be responded to and feasible solutions need to

be provided. Furthermore, the magnitude of applicable forces via laser tweezer highly depends on the refractive index of the target. In this regard, droplets need to have an index of refraction sufficiently larger than that of the continuous phase. Thus, the question arises how large the impact of optical traps on droplets really is and whether both single beam tweezers and randomly distributed trap landscapes can be successfully applied to emulsions as well.

This thesis covers four main chapters, each focusing on one aspect of my work and designed to walk the reader along the thesis' title *Microfluidic Femtoliter Droplets Exposed to Laser Potentials*. Thus, Chapter 2 starts up with some theoretical background on two-phase liquid systems, hydrodynamics and microfluidics. In addition, the physical basics and formulas for droplet formation in small channels are elaborated. Subsequently, there is the demand to build a device that features a monodisperse generation of microdroplet emulsions. So Chapter 3 goes into detail on how droplet generation chips are engineered, fabricated and improved using the soft lithography technique. The ensuing Chapter 4 focuses on the stabilization of droplet emulsions, which turns out to be an essential step to progress towards applications. Additionally, droplet and particle systems are contrasted on their phase behavior and dynamics. Eventually, Chapter 5 shows ways to laser manipulate droplets. Different approaches to calculate the laser tweezer's trap stiffness are tested. Also droplet diffusion under optical and dense particle constraints are evaluated. Finally, Chapter 6 concludes results of this work and gives sums up perspectives for further interesting studies.

## Chapter 2

# Controlled formation of droplet emulsions

To understand microfluidics one needs to learn about liquid-liquid systems and their flow in small channels. When flows run through tiny microchannels instead of large pipes, the amount of turbulences decreases. At the same time, the hydrodynamic resistance grows exceedingly and volume throughput is kept at a minimum. Interestingly, parallels from electric circuits to flow channel systems can be drawn and popular laws from this whole different branch rediscovered. However, this circumstance allows perspectives in design of fluid systems, so that for the first time one is able to study the behavior of immiscible flows when squeezing them together with high pressures. Hence, there is a set of forces involved in droplet formation which is presented. Characteristic values, as for example the capillary number, help balancing these. Furthermore, so-called jetting affects the size dimensions of microdroplet-emulsions generated.

## 2.1 Immiscible two-phase liquid systems

Biphasic systems that do not mix build up phase separation interfaces. Generally speaking, water-based, polar solutions are immiscible with non-polar solvents. Miscibility is influenced by ionic strength, pH and temperature. Yet, mixing behavior of large molecule structures is subject of complex chemistry. Due to entropic reasons (see in Sec. 4.1.3), the interfacial area between immiscible phases seeks a minimum. However, there are amphiphilic molecules that have both polar and non-polar head-groups and therefore assemble at these interfaces. Following this principle, it can be energetically favorable to increase interfacial area. By blending the liquids at a sufficient concentration of these so-called surface-active-agents (short: surfactant) molecules, droplet emulsions may become a stable condition of the system. This heterogeneous dispersion of liquids is then referred to as an emulsion.

Emulsions per-se are not energetically stable at all. Four types of mechanisms can lead to a breakdown of emulsions into completely separated phases or intermediate stages. Flocculation is "the process of contact and adhesion whereby the particles of a dispersion form larger-size clusters" [McNaught and Wilkinson, 1997] and an unwanted effect, especially when comparing emulsions to colloidal suspensions in terms of thermal motion (see Sec. 4.3.2). The thermodynamically driven spontaneous merging of liquid droplets is called Ostwald ripening [Ostwald, 1896]. This phenomena is based on the fact, that usually larger droplets are energetically more favorable than smaller ones due to their lower free energy (see Sec. 4.3). Small liquid particles therefore get absorbed while larger ones grow bigger. That is also why particularly monodisperse emulsions remain more stable. Another event disturbing an exemplary droplet dispersion is creaming or sedimentation where one phase's objects gather on the sample container's top or bottom due to density differences. All three mentioned processes increase the likelihood of coalescence which is the technical term for droplet fusion.

There are various types of emulsification processes – from simple blending, over centrifugation to ultrasonic treatment. Often the chemical stability defines the size and dispersity of forming droplets. An elegant way to design emulsions pursuant to preconceived geometries is by utilization of microfluidic technologies.

## 2.2 Low Reynolds number hydrodynamics

Before laying out channel structures that allow droplet formation, some hydrodynamic basics must be introduced. Microfluidics is based on laminar flow as it deals with small flowrates and rather viscous fluids. The dimensionless Reynolds number quantifies the degree of turbulence of a flow. Small numbers ( $\text{Re} \lesssim 2,000$ ) yield laminar flows. If  $\text{Re} \ll 1$ , there is a transition into a creeping-flow as viscous forces completely dominate the inertia forces.

Yet, microfluidic channels on a chip network often have a nearly square-like cross section area  $A$ . Due to typical wetting characteristics, the flow occupies an elliptical, nearly circular area with perimeter  $b$  and would not interfere with channel corners. The hydrodynamic diameter  $d_H$  is a geometric constant defined as

$$d_H = \frac{4A}{b} \quad (2.1)$$

Moreover, the Reynolds number depends on viscosity.  $\nu$  is the kinematic viscosity of a solution and  $\eta$  the dynamic viscosity (in some literature it is also referred to as absolute viscosity  $\mu$ ) and they are related via the fluid's density  $\rho$ , which gives

$$\eta = \nu\rho. \quad (2.2)$$

Note that viscosities are usually subject to temperature dependence, which is neglected here, since experiments are executed under a controlled room temperature environment. Appearing characteristics are the volume flowrate  $Q$ , the tube's cross section  $A$  and its hydrodynamic diameter  $d_H$ . The Reynolds number is defined as the ratio of inertial forces to viscous forces within a fluid and thus predicts fluid behavior as

$$\text{Re} = \frac{(\text{inertia force})}{(\text{viscous force})} = \frac{\rho d_H Q}{\eta A} = \frac{d_H Q}{\nu A}. \quad (2.3)$$

Microfluidic glass-capillaries (see Sec. 3.1) usually have a circular cross section with  $d_H = 2r$  with  $A = \pi r^2$  where  $r$  is the channel's radius. Then flows yield

$$\text{Re} = \frac{2Q}{v\pi r}. \quad (2.4)$$

However, in this work polymer-mold devices featuring square channels with width  $w$  are subject of study. Assuming  $d_H = w$  and  $A = w^2$ , Eq. 2.3 leads to

$$\text{Re} = \frac{Q}{vw}. \quad (2.5)$$

Typical values for operating a microfluidic chip are a flowrate  $Q = 100 \mu\text{l h}^{-1}$ , the kinematic viscosity  $\nu = 1 \text{ cSt}$  of fluorinated oil (at  $20^\circ\text{C}$ ) and channel width  $w = 20 \mu\text{m}$ . This yields a Reynolds number of 1.39, which is almost in the creeping-flow regime.

## 2.2.1 Laminar flow in microfluidic channels

The fluids relevant for microfluidics are aqueous solutions and fluorinated oils (see Chapter 4). They are non-compressible and uniformly-viscous Newtonian fluids. Some parameters depend on the system itself; others can be tuned during an experiment such as pressure  $p$  and flowrate  $Q$ . The Hagen-Poiseuille law for laminar flows in thin cylindrical capillaries connects these two values to

$$Q = \frac{\pi r^4}{8\eta} \left( \frac{dp}{dx} \right). \quad (2.6)$$

Equation 2.6 applies for a channel that is perfectly straight and infinitely long. However, if the channels length  $L$  is much greater than its hydrodynamic radius, the differential can be simplified by the pressure difference  $\Delta p$  divided by  $L$ . With the resulting finite Hagen-Poiseuille Eq. 2.7, one can calculate the pressure difference in a simple, straight microfluidic channel, if given the applied flow rate

$$Q = \frac{\pi r^4}{8\eta} \frac{\Delta p}{L}. \quad (2.7)$$

When it comes to more complex channel structures including curves, different diameters and impurity filters, the more complicated Navier-Stokes Eq. has to be solved numerically. This rigorous analysis of flow through such networks can be achieved by resorting to computational fluid dynamic (CFD) analysis.

### 2.2.2 Hydrodynamic resistance

Transferring concepts and their solutions from one branch of science to another often helps to further understand complex physical phenomena. Here, the electrical circuit theory is applied to the field microfluidic networks in order to obtain the resistance of micro-channel systems.

Ohm's law in electric circuit analysis describes the voltage drop  $\Delta U$  and the electric current  $I$  in a resistive conductor  $R_{\text{Ohm}}$ :

$$\Delta U = IR_{\text{Ohm}}. \quad (2.8)$$

The analogous equation in hydrodynamics reads as follows

$$\Delta p = QR_{\text{H}}. \quad (2.9)$$

Thus, using Eq. 2.7, the hydrodynamic resistance  $R_{\text{H}}$  [ $\text{Pa s}^3 \text{ m}^{-1}$ ] of a straight circular channel can be defined as

$$R_{\text{H, Circular}} = \frac{\Delta p}{Q} = \frac{8\eta L}{\pi r^4}. \quad (2.10)$$

For a square micro-channel one side length is roughly  $d_{\text{H}}$  which yields

$$R_{\text{H, Square}} = \frac{128\eta L}{\pi d_{\text{H}}^4}. \quad (2.11)$$

However, in this work rectangular channels play a role (see Sec. 3.4.1). These feature a low aspect ratio between width  $w$  and height  $h$  and are approached using the reciprocal estimate  $d_H = 2wh/(w+h)$  giving

$$R_{H, \text{Rect}} \approx \frac{8\eta L}{\pi \frac{wh}{w+h}^4}. \quad (2.12)$$

Since engineering improvements on microfluidic chips in this work rely on changing the ratio of rectangular channels, Eq. 2.11 gives the precise estimate. The exact solution of the Navier-Stokes Eq. is derived using a summation of Fourier series [Cornish, 1928]:

$$R_{H, \text{Cornish}} = \frac{a\eta L}{wh^3} \quad (2.13)$$

with

$$a = 12 \left[ 1 - \frac{192h}{\pi^5 w} \tanh\left(\frac{\pi w}{2h}\right) \right]^{-1} \quad (2.14)$$

which is a dimensionless parameter that depends on the aspect ratio  $w/h$ . Equation 2.13 is accurate to within 0.26 % for any rectangular channel with  $w/h < 1$  under laminar flow conditions [Morris and Forster, 2004]. Moreover, for  $w/h \ll 1$ ,  $a$  becomes 12 and therefore high aspect ratios have a hydrodynamic resistance of  $R_{H, \text{Rect}} = 12\eta L/wh^3$ .

It is important to note that the hydrodynamic resistance (Eq. 2.13) is proportional to the inverse of the channel's height cubed, while it is just inversely proportional to its width. Thus overall, the flow-resistance of a micro-channel scales to the power of four with its (circular) tube dimensions. In electric lines, the resistance is only increases to the power of two with decreasing wire dimensions.

### 2.2.3 Kirchhoff's law analogy

The flow of molecules through tubes of a microfluidic system macroscopically behaves much like the flow of electrons through a wire in an electric circuit. This convenient picture led scientists to search for analogies between both fields and verify conventional methods of electric circuit theory on microfluid hydrodynamics [Kwang W. Oh and Furlani, 2012]. It was found that, besides resistors, there is a large number of terms that can be remapped to microflows: pressure sources correspond to voltage supplies, atmospheric pressure  $p_{\text{atm}}$  can be seen as ground (GND), the law of mass (or energy) conservation conforms Kirchhoff's current (or voltage) law, and that the maximum velocity exists in flow networks as the speed of sound, and in electric circuits as the speed of light. Since Kirchhoff's laws obey the transition, resistance systems can be calculated without solving any differential equations. For a number of  $N$  resistors collectively arranged in series applies that

$$R_{\text{Series}} = R_1 + R_2 + \dots + R_N, \quad (2.15)$$

and for the hydrodynamic resistors placed in parallel it is valid that

$$\frac{1}{R_{\text{Parallel}}} = \frac{1}{R_1} + \frac{1}{R_2} + \dots + \frac{1}{R_N}, \quad (2.16)$$

where  $R_1, \dots, R_N$  are the hydrodynamic resistance values of single straight channels.

Although the electric circuit analogy is sufficient for structural considerations of a microfluidic chip, it cannot provide details about microscopic transport of molecules through channels, e.g. time-dependent flow properties or 3d-flow-fields.

## 2.3 Droplet microfluidics

The theoretical toolbox introduced above is applied to establish a controlled low volume fluid system that handles two liquid phases and dispenses an emulsion through one gathered output. Figure 2.1 shows a microfluidic chip. It is transparent for microscope light which

makes processes inside easily observable. The mixing takes place in the micrometer-sized channel structure between glass and poly(dimethylsiloxane), forming droplet emulsions of arbitrary dimension and throughput. Practically, one inlet embodies an aqueous solution and the other an immiscible oil. To disperse one phase within the other, the interfacial tension between both liquids is lowered by adding a surface active agent (see Sec. 4.1).

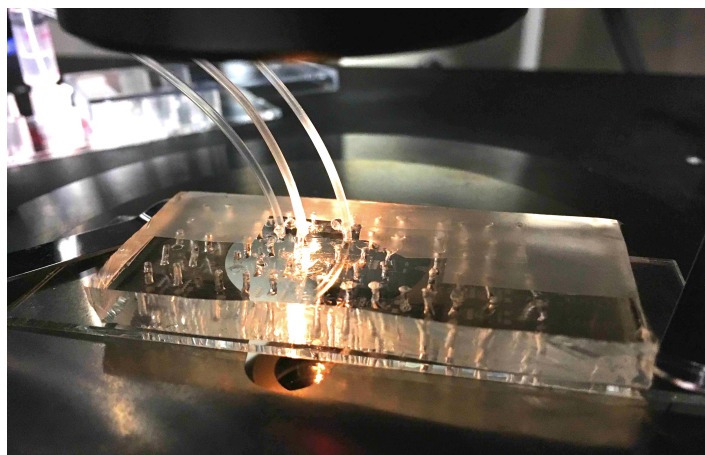


Figure 2.1: Microfluidic droplet generation chip with two attached inlet tubes (both left) and one outlet tube (right).

### **2.3.1 Flow focusing**

Droplet formation in microchannels occurs when the pressurized immiscible phases meet at a channel flow focusing junction in a certain angle and leave together through a small exit orifice (see Fig. 2.2). The angle can vary between a  $45^\circ$  to  $90^\circ$  cross flow and a  $180^\circ$  counter-flow. However, the interfacial force between the fluids keeps both phases apart until dramatically increased pressure at the exit orifice overcomes their interfacial tension. Thus, the dominant phase cuts off a small volume from the other phase's flow. As a result, it becomes energetically favorable for the less dominant phase to form spherical objects within the outer phase. These spherical objects are called droplets and scale in the order of the orifice's diameter. The flow is then referred to as being in the flow-focusing regime.

### 2.3.2 Capillary and Weber number

There is a set of parameters that characterize forces involved in droplet formation at microfluidic cross junctions. A key parameter represents the capillary number, which points out the relative importance of viscous stresses versus capillary pressure. Here,  $G$  constitutes the shear rate-of-strain in the flow field,  $d$  the characteristic length (or droplet diameter) and  $\sigma$  is the surface tension.

$$\text{Ca} = \frac{(\text{viscous force})}{(\text{capillary force})} = \frac{\eta G d}{\sigma}. \quad (2.17)$$

Typically, the capillary number ranges from  $10^{-3}$  to  $10^1$  in microfluidic droplet setups [Christopher and Anna, 2007].

Considering droplet breakup, Moritz Weber (1871-1951) postulated the critical impact of ratio between kinetic and surface energy of multiphase flows in droplet formation. Accordingly, the dimensionless quotient of inertia and surface tension is called Weber number (Eq. 2.18). It depends on the dispersed liquids density  $\rho$  and scales with the velocity  $v$  squared.

$$\text{We} = \frac{(\text{inertia force})}{(\text{capillary force})} = \text{We Ca} = \frac{\rho v^2 d}{\sigma}. \quad (2.18)$$

The Capillary number reflects the ratio between a continuous phase's drag (pulling the droplet downstream) and the surface tension (resisting the flow in the jet) before breakup happens. However, the Weber number becomes important when describing the behavior if very little viscous drag is present (so the capillary number is low). In this case, it is the inertia force of the fluid that must overcome surface tension forces and ultimately leads to pinch-off. The boundary between dripping and jetting (Sec. 2.2) is defined by the regime when the sum of both numbers is approximately 1 [A.S. Utada and Weitz, 2007].

### 2.3.3 Jetting effects

Jetting occurs when surface tension outweighs the flow focusing pressure, which induces the droplet cutoff [Sullivan and Stone, 2008]. Figure 2.2<sup>1</sup> shows the jetting effect that appears at different flowrate ratios or surfactant fractions, respectively. The usual case is the controlled breakup, 2.2 (a). The formation of droplets is controlled by the continuous phase's blockage of the orifice, which resultantly causes an increased pressure behind the flow focusing junction where the pinch-off takes place [Piotr Garstecki and Whitesides, 2004]. Droplets form homogeneously, occupying the whole given channel space. The dripping regime, 2.2 (b), occurs when the flowrate ratio is less balanced, generating smaller droplets due to a shifted point of breakup of the dispersed phase. There are two more regimes that fall under jetting considerations: Figure 2.2 (c) shows the narrowing-jetting regime that can form small but homogeneous droplets under finely controlled flow ratios. The breakup point is moved even further away from the orifice. The widening-jetting regime occurs when pressure is distributed heterogeneously or surfactant is lacking. Then droplets are produced relatively large, instable and thus polydispersely, or both phases can coexist without forming droplets at all.

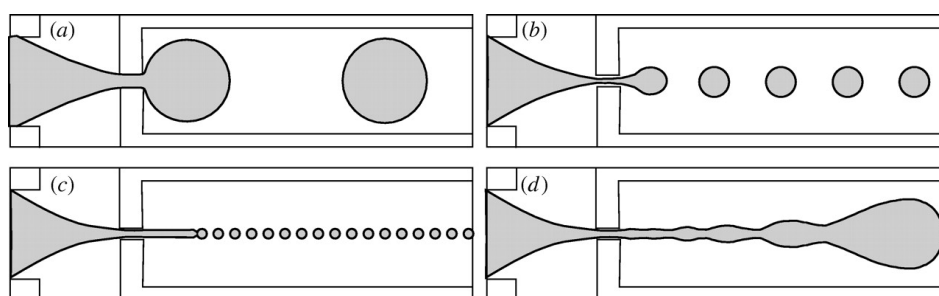


Figure 2.2: Droplet formation regimes: (a) controlled breakup, (b) dripping, (c) narrowing-jetting, (d) widening-jetting.

Through variation of the inlet phases' flow pressures, one can induce different regimes and thus form various droplet sizes within one channel geometry. Using this principle, a polydispersity in samples may be generated.

<sup>1</sup>Figure by [Sullivan and Stone, 2008]

## **Chapter 3**

# **Construction of a microfluidic platform for femtoliter droplet generation**

After the previous chapter guided through the theoretical concepts of emulsion generation, here, techniques to apply these ideas are elaborated. The goal is to fabricate a hand-held device featuring on-demand formation of micrometer size droplets, that can compete with properties of colloidal particles commonly used in experiments. Accordingly, two design concepts are introduced. From these, polymer mold devices provide the greater potential for droplet miniaturization below the current lowest limit of ten micrometers in width. Following this track, the reader is introduced to lithography fabrication steps and methods for solvent phase injection in experimental set-ups. With knowledge on how to construct chips, their resistance can be practically calculated. Noticing that pressures have to be increased vastly for miniaturizing down to femtoliter droplets, a two-layer chip is presented.

### 3.1 Glass-capillary and polymer-mold devices

In 2001 the first time monodisperse droplets could be produced within a microfluidic chip made of polyurethane [Olaf Wagner and Haag, 2016]. There are two customary microfluidic device categories. One class is represented by glass-capillary devices. Thus, a cylindrical glass tube with a small orifice is brought into a larger capillary. In the simplest configuration shown in Fig. 3.1<sup>1</sup>, the dispersed phase (called Inner Fluid) is injected in the opposite direction to the continuous phase (called Outer Fluid). Hence, this technique is referred to as counter-flow. The injection pressures of both fluids need to be balanced in a way that they are forced to flow through the small orifice in the center. Due to their immiscibility, the outer fluid then cuts off drops from the inner fluid. Accordingly, the system is considered to be in a flow-focusing regime where the droplet size is set by the flow ratio between both phases. Glass capillary devices are an option for simple mixing architectures and provide high durability in terms of pressure resistance as well as thermal and chemical stability [Whitesides, 2006]. These devices are usually hand-made and hard to be fabricated in a reproducible way.

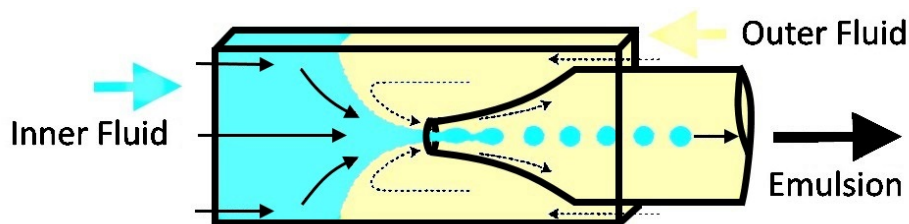


Figure 3.1: Scheme of a glass micro-capillary device in the counter-flow-focusing regime.

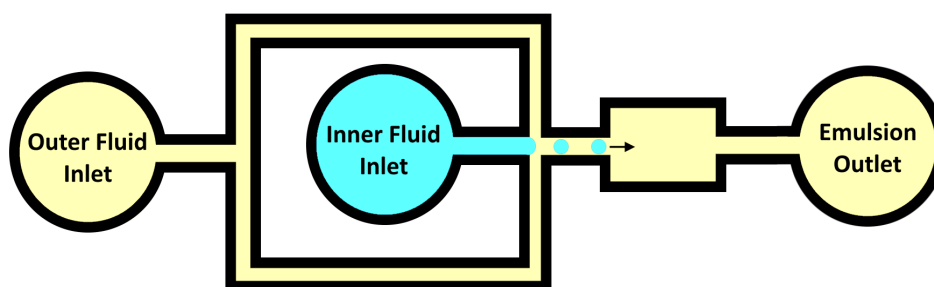


Figure 3.2: Drawing of a polymer-mold device's channel structure in the cross flow focusing regime.

<sup>1</sup>Figure by [A.S. Utada and Weitz, 2007].

Polymer molding is a technology for easy prototyping and features potential for mass production. Figure 3.1 portrays an exemplary fluid channel structure yielding droplet formation (top view). The circles correspond to holes in the chip where inlet and outlet tubing is attached. Flow runs from the left to the right towards the outlet and droplets form at the cross flow junction. This is the critical area where the perpendicular flow (yellow) cuts off the horizontal flow (blue). Due to the previously mentioned parallels to semiconductor physics, one came up with the idea of building microfluidic chips using similar techniques. Hence, the analogous process is called soft lithography. A major advantage of chips fabricated this way lies in a fine feature size down to nanometer resolution, while the minimum existing orifice diameter in glass-capillary devices is about five micrometers. Another upside is the possibility of individually designing the channel structures using a computer CAD software. With this tool, insertion of extra inlet resistors to establish a stable flow towards the droplet generating junction (considering there are fluctuations in the pump/pressure injection system), creating filters to avoid channel clogging due to dirt, and even adding a chamber for on-chip manipulation of generated droplets is possible. For the manufacturing of soft matter microfluidic chips, it is common to use polydimethylsiloxane, typically also referred to as silicone. The following chapter covers the chip fabrication in detail (Sec. 3.2) as well as the composition of the injection phases (Sec. 4.1).

## 3.2 Soft lithography chip fabrication

Polydimethylsiloxane (PDMS) is an organic polymer consisting of repeating  $\text{Si-O-(H}_3\text{C)}_2$  units as shown in Fig. 3.2<sup>2</sup>. It is optically clear, non-toxic and non-flammable, which gives PDMS the potential to be used in most medical and domestic applications. PDMS is able to replicate features as small as 30 nm in size [Xia and Whitesides, 1998].

The soft lithography process is executed in a series of steps which can be classified in three categories. It starts with a transparency photomask that is individually designed to match the purpose of the application. Utilizing the photomask, a mold is assembled onto a silicon wafer (Sec. 3.2.1) composed of cross-linked photoresist. The usual process consists of spin coating, soft baking, exposure and post exposure baking (PEB), followed by developing of the epoxy-photoresist. Each step is discussed in the following section. The final product is

---

<sup>2</sup>Figure drawn using molview.org.

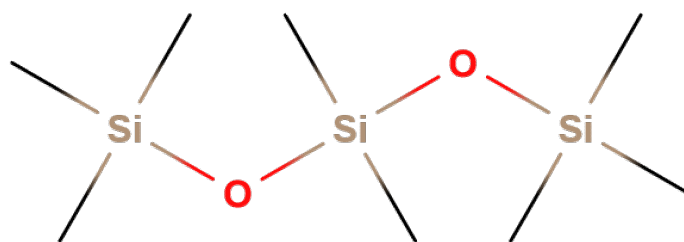


Figure 3.3: Structure of Polydimethylsiloxane.

then called master and used for replica molding (Sec. 3.2.2). Here, PDMS in its liquid state is poured onto a silicon mold. After polymerization, the PDMS stamp is bound onto a glass slide. For the insertion of the emulsion phases via millimeter tubing, small holes are punched through the PDMS layer.

The following sections guide through the process in all the details. Thus, it can be viewed as a general instruction for the reader to perform microfluidic chip molding in a soft materials cleanroom.

### 3.2.1 Master assembly

The development of a microfluidic chip begins on the computer using a computer-aided design software AutoCAD (Autodesk) for drawing channel structures. Drawings are then processed on plastic transparency photomasks (here printed by CAD/Art Services, Inc). Figure 3.4 shows a typical CAD drawing created for a droplet generating chip used in this work. Looking at the drawing, flow goes from left to right. The white structure is transparent for ultraviolet-light in the printed photomask, thus becoming the fluid channel after fabrication. Three white circles in the figure mark points where two inlet and one outlet tubing is inserted through the PDMS mold. Microfluidic channels easily clog due to small particles in the system. Clogging immediately interrupts stable flow conditions and hence uniform droplet generation. There are filters for the inlet channels to block small pieces of dirt and dust that tend to end up inside the system through reagent contamination or dirty equipment, even though chips are fabricated in a cleanroom environment. The curved channel structure in the outer phase helps with flow stabilization, especially when working with a flowrate-based injection that can be discontinuous (see chapter 3.3.2).

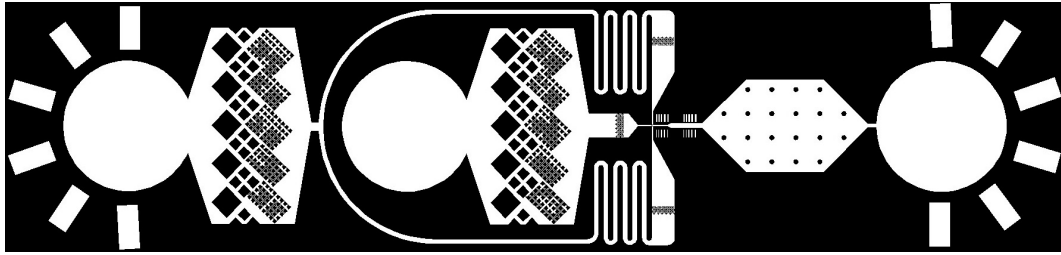


Figure 3.4: CAD drawing of a photomask. The white features allow ultraviolet-light to pass through.

Figure 3.5 shows a closeup of the cross flow junction located in the center, slightly to the right, in Fig. 3.4. The depicted section is the critical domain that defines the resulting droplet's size. By altering the cross junctions width, the diameter of formed droplets is defined. In one photomask design several geometries can be included, fitting on one wafer. In doing so, a chip capable of producing a range of droplet sizes is built.

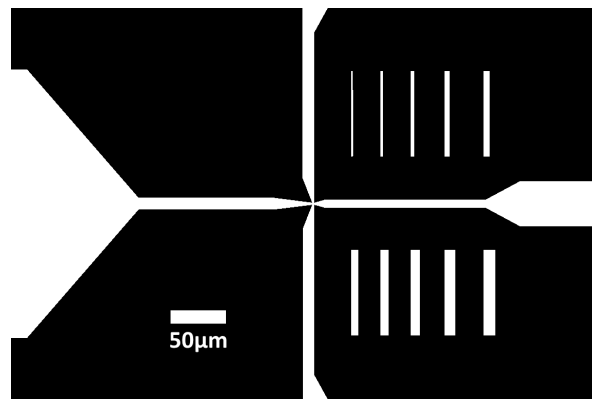


Figure 3.5: Zoom on the cross junction area in the center of Fig. 3.4.

The following steps are done using chemicals in a dust-free environment, ideally a clean-room. Figures 3.6 to 3.11 illustrates the creation of a microfluidic chip during preparation.

Figure 3.6 shows the application of an even layer of liquid SU-8 photoresist on a silicon wafer. Thus, the fluidic channel mold is fabricated via photolithography by chemical development of specific photoresist (Microchem SU-8 2000.5 - 3000) on a 2- or 3-inch silicon wafer in step (a). Depending on the intended layer thickness, its viscosity and the spincoating frequency defines the channel depth of the posterior chip. Due to reproducibility, it is important to exactly follow the instructions the manufacturer recommends. However, exact time indications are fine-tuned with tables Microchem provides [Microchem Corp Newton MA, 2016]. As shown in step (b), SU-8 is poured onto the wafer. The epoxy-based, negative

photoresist (SU-8 2000 to 3000) comes as a viscous polymer liquid. Negative means that the UV-exposed area stays on the substrate, while the rest is washed away during development. Microchem provides the recommended program parameters to achieve the intended layer thickness. Low viscosity liquids spread further during spinning and thus form a thinner layer. The SU-8 3000 series has a variety of photoresists with viscosities from 65 cSt to 12,000 cSt. Therefore, it is used for film thicknesses between 10  $\mu\text{m}$  and 120  $\mu\text{m}$ . For formation of droplets, whose size are sufficient for optical tweezers manipulation, thin channel structures smaller than 10  $\mu\text{m}$  are necessary. SU-8 2000 series provides viscosities as small as 2.49cSt (SU-8 2000.5) which allows twelve different film thicknesses reaching down to 0.5  $\mu\text{m}$ . For layers of 4  $\mu\text{m}$  that were fabricated for this work, SU-8 2002, which has a viscosity value of 7.5 cSt, is used. Handling this liquid is comparable to the pouring of water, whose value is about 1cSt at room temperature. A drop (about 1ml per inch substrate diameter) of SU-8 is applied on the clean wafer. The centrifugal force of a spin-coating instrument (2,000 to 3,000 rpm depending on thickness) distributes the photoresist homogeneously thick across the area in step (c).

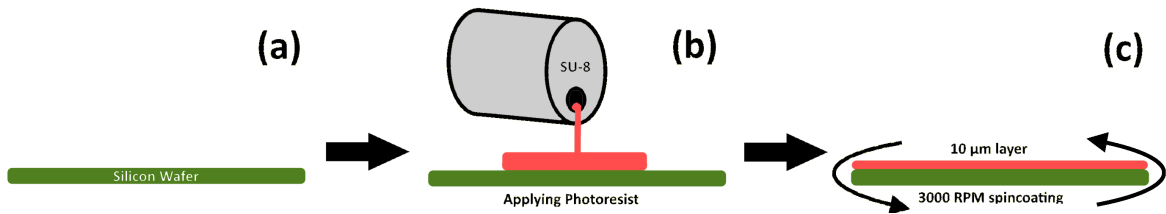


Figure 3.6: Steps a), b) and c).

Figure 3.7 schemes how an ultraviolet lamp cures designated structures on the wafer defined by the partly transparent photomask. Therefore, the wafer is placed on a level hotplate with accurate thermal control at 65  $^{\circ}\text{C}$  and 95  $^{\circ}\text{C}$ , respectively, for about 1 min, step (d). Built up photoresist on the substrate's edges is washed off to guarantee closer contact of the photomask in step (e), which improves resolution. Then, the photomask designed in section 3.4 is fixed onto the substrate by putting it on a transparent glass sheet tightened with screws. To crosslink the photoresist's molecular chains, the whole substrate is exposed to UV light of 60 to 160  $\text{mJ}/\text{cm}^2$ . Therefore, a calibrated UV lamp ( $< 350 \text{ nm}$ ) with  $P = 13 \text{ mW}$  is placed above the wafer for an estimated time of about 10 seconds. Light only reaches through transparent domains of the photomask. After half of the exposure time, the sample is rotated for more homogeneous coverage of the surface area. The glass slide can then be detached. Features become slightly visible by eye after the postbake process in step (f) which is similar to softbaking, though time varies.

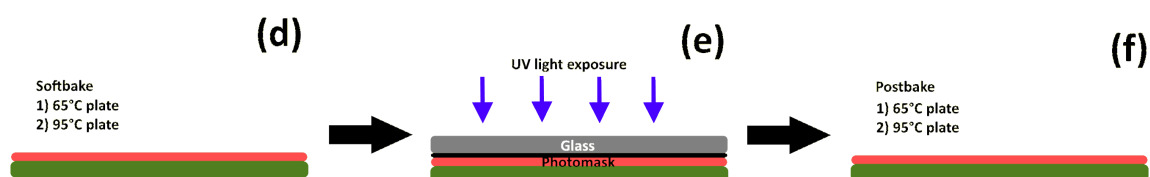


Figure 3.7: Steps d), e) and f).

Figure 3.8 demonstrates how the non-polymerized SU-8 is washed off so the channel structure can be negatively replicated in PDMS. In order to do so, the sample is developed and rinsed in propylen-glycol-monomethyl-ether-acetate (PGMEA) for 1 to 5 min in step (g). After being washed with isopropanol and air-dried, remaining acid evaporates, while the wafer rests in the oven at 200 °C for 2 min in step (h). An optional hard baking step, taking up to 30 min, in an oven of 150 to 250 °C, enhances the mechanical resistance. This is not essential for our purpose, since one works with the PDMS stamp after all. After step (h), the structure that was previously designed on the computer remains as a negative on the silicon substrate for molding of PDMS chip replicas. Since many microfluidic chips can be polymer-molded using this stamp, a petri dish containing the silicon wafer is then referred to as chip master.

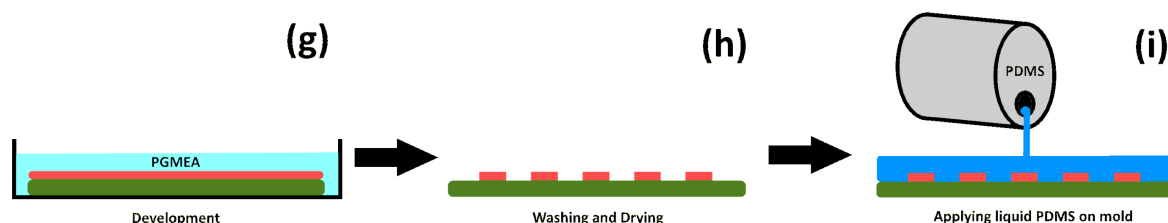


Figure 3.8: Steps g), h) and i)

### 3.2.2 Replica molding

Figure 3.8 (i) demonstrates the first step in replica molding from a chip master. Therefore, PDMS (Sylgard 184 Dow Corning) is mixed at the standard 1:10 mass ratio and poured over the mold within its petri dish. To avoid entrapment of air bubbles inside the PDMS, it is degassed for at least one hour under vacuum before it cures at 65 °C overnight (12 to 18 hours). Usually the following steps are performed the next day.

After PDMS is cured, it can be detached and prepared for bonding to glass using oxygen

plasma. Thus, as Fig. 3.10 indicates, the PDMS replica is cut along the edges on the wafer using a scalpel and thereupon peeled off in step (k). Fluid in- and outlet holes are formed with a biopsy punch (0.75 mm Harris Uni-Core) in step (l). Figure 3.9 demonstrates what the PDMS stamp looks like after it is cut out of the petri dish and peeled off the wafer, and before plasma bonding it to a glass bottom. In the background of the image lies the used biopsy punch. Since the stamp is turned around, on a closer look, the thin channel structure is visible.



Figure 3.9: Microfluidic chip's PDMS stamp after step (l) and before bonding to glass.

Figure 3.10 (m) shows the PDMS piece being bound to glass using an oxygen plasma treatment. Before exposing PDMS and glass to plasma, both need to be cleaned with air pressure. Additionally, adhesion tape is affixed and peeled off to remove all remaining dust particles. The set of pieces is placed inside a plasma oven (Plasma Prep 2) that is first degassed and later flooded with oxygen for around 2 min until the pressure settles. Plasma is generated for 10 s at 20 to 35 W (here often 25 W). The power values base on experimental values that are registered in a list referring to the prevailing bonding components (glass/PDMS or PDMS/PDMS). As introduced above PDMS material consists of repeated units of  $\text{O}-(\text{CH}_3)_2$ . Under oxygen plasma exposure these develop silanol groups ( $-\text{OH}$ ) at the expense of methyl groups ( $-\text{CH}_3$ ). The oxygen plasma increases the surface concentration of hydroxyl groups which have a higher amount of free energy than unoxidized PDMS [Chaudhury and Whitesides, 1991]. This leads to the formation of strong intermolecular bonds. The silanol groups are polar in nature, so the exposed PDMS surface becomes highly hydrophilic. A relative change in the advancing contact angle of deionized water can be observed [Shantanu Bhat-

tacharya and Gangopadhyay, 2005]. Accordingly, the silanol groups condense with those on another surface where two such layers are brought into conformal contact. However, covalent bonding creates a tight irreversible seal between both layers.

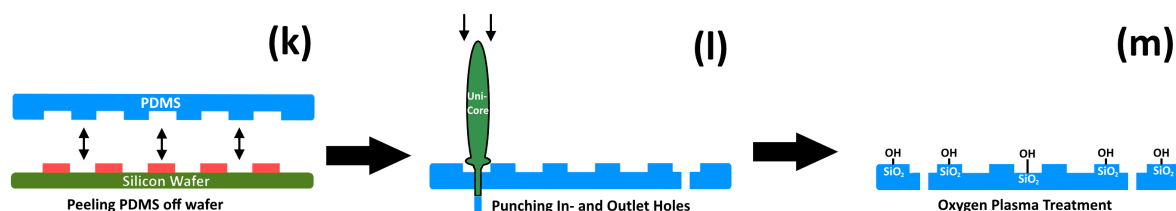


Figure 3.10: Steps k), l) and m).

Figure 3.11 shows the completion of a microfluidic chip. After careful attachment of a microscope glass slide in step (n), the chip rests for a couple of hours at 65 °C. Mounting the glass is sensible to manually applied pressure. If pushing too much, channel structures adhere completely on the glass making flows in later experiments impossible, and, if no pressure is applied the PDMS and glass surfaces do not seal correctly. Step (o) demonstrates the insertion of two inlet (one for each phase) and one outlet polyethylene tubing (SCI, inner diameter 0.38 mm, outer diameter 1.09 mm) through punched holes in PDMS.

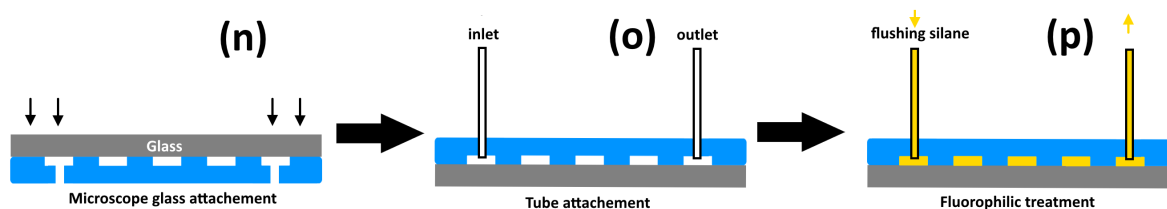


Figure 3.11: Steps n), o) and p).

About an hour after plasma treatment, glass and PDMS entirely return to their original adhesion behavior. For the application of fluorinated oil as the continuous phase, a fluorophilic treatment is necessary to ensure consistent wetting of both surfaces. PDMS is a naturally hydrophobic elastomer while glass is hydrophilic. For this work, fluorocarbon oil (3M HFE-7500) is utilized as the continuous phase. The oil has an affinity for the PDMS surface and avoids contact with the glass. To achieve a smooth wetting of the device on both interfaces, the channels need to be treated with fluorophilic silane. The silane used is a 1H,1H,2H,2H-Perfluorooctyltrichlorosilane mixed with 2 wt% in HFE-7500 fluorocarbon oil. After setting up a chip with the attached inlet tubing of the oil phase, a syringe containing the silane-oil-mixture manually injects just enough fluorophilic solution until the channel structure is

homogeneously wet, see in Figure 3.11 step (p). The experiment starts right after this process to make sure that the silane is being flushed out properly. Leaving silane rests within the channels can cause clogging of smaller structures due to assembly of silane molecules.

In most recent experiments involving channel structures smaller than ten micrometers use of silane is renounced. A couple of hours after flushing, formation of silane aggregates, that are not stopped by filters and can clog tiny channel junctions, is experienced. Wetting of the fluorinated oil phase is still sufficient for femtoliter droplet generation. Silanization of microfluidic channels remains a standard procedure in many other applications.

Besides the channel width and length, which are determined by the photomask design, the channel height (z-component) is a parameter that substantially affects the chip's resistance. Since some parameters during fabrication might differ by chance, e.g. exact timing or calibration of the UV lamp, it can be helpful to measure the channel height via 3D confocal microscopy after chip preparation. A standard confocal instrument (Resonant, Zeiss Instruments) focuses on the upper glass interface and the z-value is noted. The difference in z-value to the PDMS boundary layer (where the channel structure is focused on) gives the channel height. Subsequently, the chip's properties are further validated in order to improve the design of the next photomask and to exterminate physical weaknesses. However, experiment and fabrication are reciprocal procedures during microfluidic chip development. For this thesis many design and fabrication tries were performed until a feasible master for miniature droplet generation chips could be accomplished.

### **3.3 Microfluidics: injection and acquisition**

Flow speeds in microfluidics depend on the phase injection. Usually droplet formation is not-observable by conventional microscope cameras or human eye. However, two options for pumping reagent into a microfluidic chip are investigated. Both methods involve attachment of polyethylene tubing to syringes (Becton Dickinson) containing the reagent compositions.

### 3.3.1 Image acquisition

The droplet breakup occurs on a timescale of milliseconds. To investigate droplet elongation in order to estimate surface tensions, a high-speed camera (Allied Vision Mako U-130B) is attached to an inverted microscope. By decreasing the region of interest from 1280x1024 to 600x64 pixels the framerate (measured in fps or Hz) could be scaled up from 168 fps to over 2000 fps. Theoretically, the framerate is limited by the shutter time of 44.2 microseconds which leads to a rate of 22,600 fps with perfect lighting. In practice, 1000 fps could be well reproduced with a standard deviation of 10 fps due to hardware limitations in signal processing.

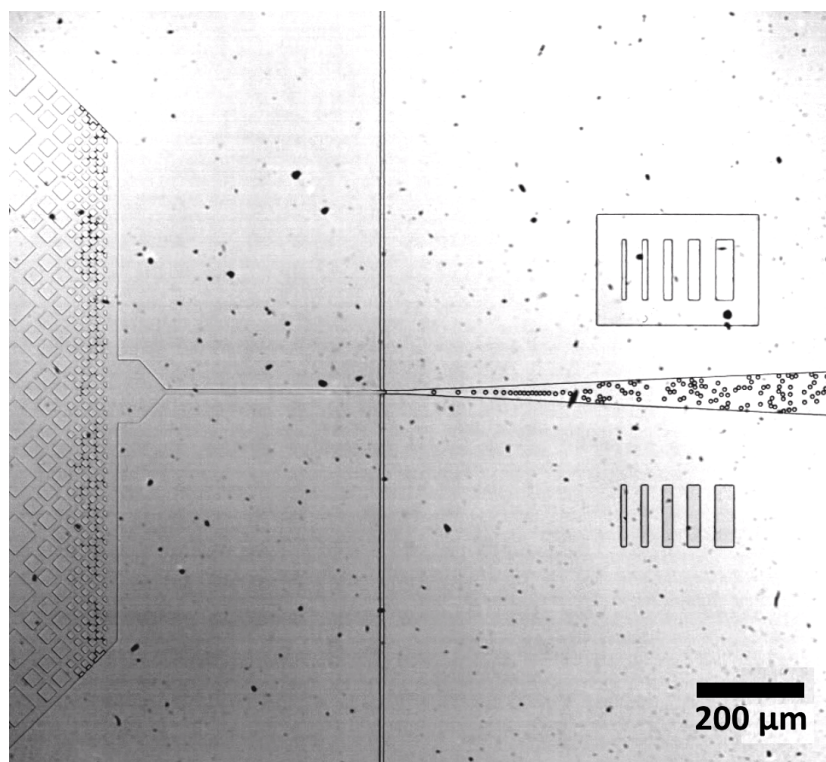


Figure 3.12: Operating cross flow focusing design forming w/o emulsions.

Figure 3.12 shows a microscope image of the chip captured in the flow-focusing regime. The oil phase is the continuous phase, therefore its flow channels split up and enter the image from the top and the bottom. The dispersed phase (deionized water with 60% sucrose) comes from the left. Consequently, aqueous droplets in oil (w/o) are generated. The droplet nozzle has a cross section of  $7\ \mu\text{m}$  times  $7\ \mu\text{m}$ , forming droplets of about  $8\ \mu\text{m}$  in diameter. The ratio between the orifice dimensions and droplet diameter is slightly increased due to jetting

effects (see 2.3.3). At the very left parts of the dust filter are visible. Above and below of the stream, which is directed to the right, size bars give a quick estimate of resultant droplets' dimensions.

### 3.3.2 Volume-driven flow

Figure 3.12 is operated using a volume-driven flow with rates of  $15 \mu\text{l h}^{-1}$  for the dispersed phase and  $75 \mu\text{l h}^{-1}$  for the continuous phase. A ratio of 5:1 performs well in experiments. Otherwise, jetting might perturb the uniformity of the droplets. Commonly used are syringe infusion pumps (Harvard Apparatus). These feature a slowly rotating screw that pressurizes the clamped syringe. For the purpose of this work, flowrate-based injection has some major disadvantages, which are primarily critical in high resistance chips. For small rates of  $Q < 10 \mu\text{l h}^{-1}$ , the screw does not rotate continuously. The pump then only increases pressure in regular time steps. This is a sign that the lower limit for operating the pump is reached. However, it causes batch wise flow in the chip. This effect becomes visible at high resistances when small droplets inside the channel flow back and forth. For compensation some extra resistor channels (180 degree curves) are drawn onto the photomask (see Fig. 3.4). These channels look like coils in an electric circuit. In fact, their purpose is very similar to its analogy, since coils delay hydrodynamic flows, making them more stable and continuous. Another problem to face is the missing control of pressure inside the chip. A clogged channel can cause detachment between PDMS and glass. It results in irreversible demolition of the whole chip and spills reagent.

### 3.3.3 Pressure-driven flow

In a pressure-driven injection set-up, each reagent syringe is attached to the lab's air pressure socket with a valve for regulation. Therefore, each phase can be operated with different pressure levels. Figure 3.13 shows a photo of the pressure set-up constructed for this work. The lab's pressure socket connects with the right end of the y-piece. Two inlet valves allow finer regulation of both inlet phases' pressures. The two ends of the y-piece are connected via an adapter with standard infusion syringes. These are equipped with  $0.2 \mu\text{m}$  syringe filters and 0.5 mm needles (Luer-Lock system). The needles are plugged into 0.38 mm inner diameter polyethylene tubing that is attached to the microfluidic chip on the other end.

The volume flowrate then depends on the chip's hydrodynamic resistance. For operating a microfluidic chip, maximum pressure values of 2 bar (29 psi) are recommended in order to not damage its structure. Overall, the pressure-driven set-up has proven advantageous due to its finer control. By measuring the amount of reagent through the outlet, experimental values, e.g. the hydrodynamic resistance can be calculated using Eq. 2.13.



Figure 3.13: Adjustable pressure valves attached to inlet phase syringes on the other end.

### 3.4 Miniaturization to femtoliter droplet regime

The common droplet size occurring in biomedical engineering applications ranges from 100  $\mu\text{m}$  to 10  $\mu\text{m}$  diameter. For encapsulation of cells or chemical reactions on a small scale, this size seems sufficient. However, gravitational forces of droplets this large exceed optical tweezer effects drastically. Thus, it is aimed for droplet diameters close to those of colloidal

particles. Droplets can then be compared with a variety of polystyrene particles with 8  $\mu\text{m}$  diameter and lower, where previous measurements were performed on [Sebastian Horstmann and Egelhaaf, 2016].

The set of tools introduced in this work considering droplet minimization involves two techniques: balancing the flowrate (and, respectively, the surfactant fraction) to get into a narrowing jetting regime (see Sec. 2.3.3), however appears rather volatile in experiments. Accordingly, decreasing the geometries where droplets form is a more solid approach. As it was shown in Sec. 2.2.2, shallow chips with less than 10  $\mu\text{m}$  in overall channel height show exceedingly high resistance causing almost zero flowrate at critical pressure. This is due to the inverse proportionality of the hydrodynamic resistance to the third power of the rectangular channel's height (see Eq. 2.13). For miniaturization from pico- to femtoliter volume droplets, some tricks need to be applied.

In 2013, Wang succeeded in producing droplets as small as 5.5  $\mu\text{m}$  in diameter, utilizing a PDMS chip with a so-called normally-closed microvalve [Wang and Lee, 2013]. This technique allows to generate droplet volumes dependent on applied pressure. However, the advantage of solid PDMS chips lies in the fact that inlet pressure scales with throughput while the droplets size remains predefined (considering jetting is not an option). Thus, sticking to conventional PDMS on glass designs, it is tested, whether Wangs results are reproducible.

### 3.4.1 Two-layer chip design

Flow pressure drops proportionally with its channels length. Since sections of small channel diameter cannot be avoided when attempting to form micrometer droplets, these are kept very short. The possibility to do soft lithography multiple times for fabrication of an enriched three-dimensional structure presents a huge advantage. The ability to have a two-layer device allows to build a shallow cross flow junctions, but deep supply channel structures. Thus, all flow sections relevant for droplet size are minimized and everything else is left feasibly large to make the least compromises concerning flow resistance. Because supply channels have a comparatively low hydrodynamic resistance, the shallow cross flow junction then defines the whole chip's resistance. Figure 3.14 illustrates how droplets are generated in a pancake shape and then emerge to spherical shape. This trick reduces their sizes within the given photomask resolution limit of 10  $\mu\text{m}$  vastly.

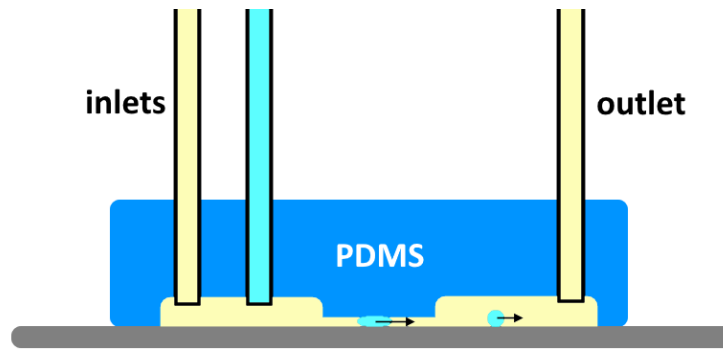


Figure 3.14: An illustration of deformed droplet generation in a two-layer chip.

The fabrication of a two layers chip needs two standard plastic transparency masks, each containing either just the supply channels or just the cross junction. The soft lithography process is now implemented in two steps. The thin layer features just the flow focusing cross junction. Thus, its photomask solely contains a structure such as the one shown in the closeup in Fig. 3.5 and some alignment marks. After the development of this first shallow 3  $\mu\text{m}$  layer, the remaining structures are produced separately with a more viscous photoresist and a second photomask. The higher viscosity yields a thicker, but just as homogeneous, photoresist layer of 10  $\mu\text{m}$  on the wafer after spin-coating. Hence, the second photomask contains the inlet and outlet channel structure and the same alignment marks as the first one. The thin wafer structures from the first step, however, are not visible to the eye, so a mask aligning instrument helps to adjust the cross junction structures on the substrate with the second photomask. The mask aligner (ABM, Inc.) is basically a light microscope featuring precise two-stage control (x-,y-,z-axis and rotation), a fixture for the substrate and built-in UV-lamp.

After a successful fabrication, experiments with the prepared chip demonstrate that droplets are restrained by the channel's bottom and top, so that they emerge in cylindrical shapes. This circumstance keeps inner-phase volume at a minimum during generation. Figure 3.15 shows a microscope image of the aligned area where generated droplets reshape while conserving their volume. Pancake droplets that are formed in the shallow cross flow junction with 10  $\mu\text{m}$  width and 3  $\mu\text{m}$  height emerge to spherical droplets with less than 7.7  $\mu\text{m}$  in radius. Thus, droplet volumes decreases by 122% compared to spherically generated 10  $\mu\text{m}$  diameter droplets.

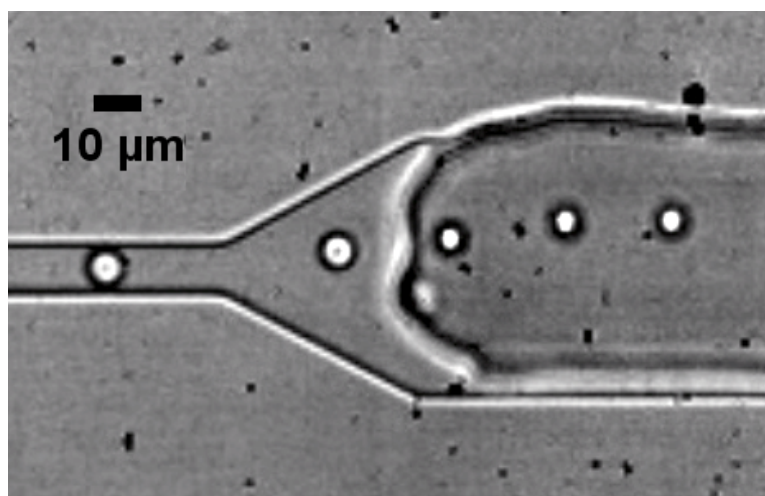


Figure 3.15: Generated pancake droplets (left) reshaping to spherical droplets (right) when channel height increases.

### 3.4.2 High-precision chrome photomask

To further improve minimization, it is aimed for a decrease in the 2d-feature's width as well. Figure 3.16 shows a high quality chrome photomask that was made for this work. The fine features are sputtered on thin glass, guaranteeing 1 µm accuracy. However, the matrix of cross flow junctions is still visible by eye. All features containing the cross flow geometry are fabricated with this improved precision photomask. In contrast to this, the conventional transparency plastic photomasks allow 10 µm precision, which is still sufficient for the residual channel structures.

Using the same method as in the previous section, soft lithography is done in two steps again. Photomasks a) and b) in Figure 3.17 each include one layer's design, which is combined on one chip. In fact, there are eleven different droplet generation geometries per chip and four of each size. Thus, the structure in a) holds an eleven times four matrix. The sizes match typical colloids (radius of 0.8, 1.05, 1.4, 1.5, 2.1, 2.5, 2.9, 4.1 µm) and in between. The supply channel structure in b) is the same for every matrix element. The high precision mask was ordered for a), features from b) can be fabricated using a standard plastic transparency photomask. All chips used for experiments that contributed to this work are since built in this two-layer design. Alignment features are included in the drawings (see the circled crosses on both photomasks) to help with orientation.

Provided that the cross flow dimension proves to emerge droplets in exactly its geometrical



Figure 3.16: High-precision chrome photomask holding only the cross flow junction features critical for femtoliter droplet formation.

measures, the resulting chip is capable of producing particles as small as  $0.8 \mu\text{m}$  in radius.

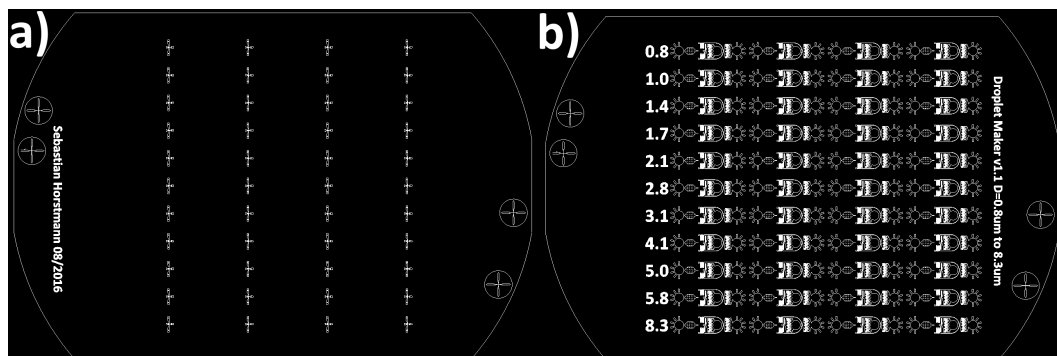


Figure 3.17: Actual two-layer photomasks. a) contains only the flow-focusing cross junction, while b) holds supply channel structure.

### 3.4.3 Overall hydrodynamic resistance

For an exemplary experiment on a two-layer chip, a resistance analysis is performed by measuring the flowrate, while keeping track of  $\Delta p$  set on the pressure valve. Equation 2.9 then gives an estimate for the overall hydrodynamic resistance of the chip.

To determine size and velocity of droplet flows a computer software is used [Basu, 2013].

DMV (droplet morphometry and velocimetry) analyses video files of droplet dynamics captured with a high-speed camera. The code is written in MatLab and makes use of particle tracking with background subtraction. Figure 3.18 shows the radius distribution of a droplet generation experiment based on a cross flow focusing junction measuring 4.1  $\mu\text{m}$  in width. A mean radius value of 1.66  $\mu\text{m}$  was deduced from 63 droplets in less than one second. The standard deviation  $\sigma$  of 0.044  $\mu\text{m}$  (equals 2.88%) can be discerned, so that monodispersity is to be assumed. The analyzed images were captured at 4025 fps.

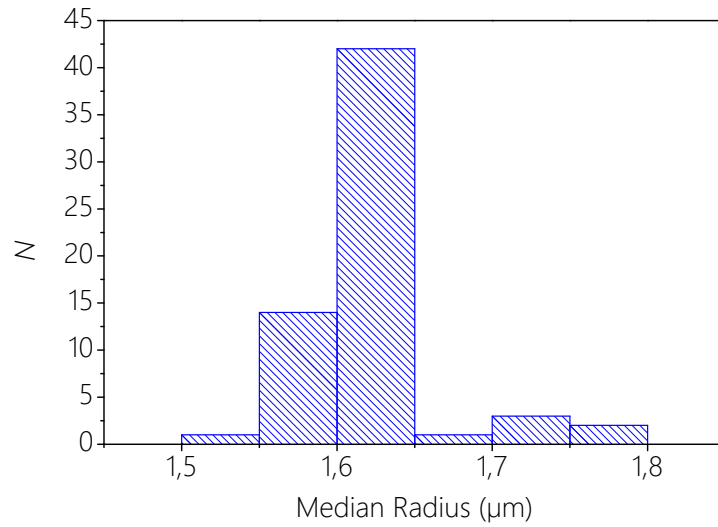


Figure 3.18: Size histogram of  $N=63$  droplets, mean radius is 1.66  $\mu\text{m}$  and  $\sigma$  is 0.044  $\mu\text{m}$ .

According to Fig. 3.18, droplets on average have a volume  $V$  of  $(17.6 \pm 1.46)$  fl in this population. Looking at Fig. 3.19 the number  $\Delta N$  of droplets formed in a time interval  $\Delta t$  can be read and so the total throughput of the aqueous phase can be derived. The number of droplets that evolved over an experimental time of  $\Delta t = 0.722$  s is 63. From all detected droplets, 15 already were inside the channel when recording started. Thus,  $\Delta N = 48$  droplets formed in the designated timeframe. The volumetric flowrate  $\Delta Q$  computes to  $(1.17 \pm 0.10)$  pl  $\text{s}^{-1}$  using

$$\Delta Q = \frac{\Delta V}{\Delta t} = \frac{4}{3}\pi r^3 \frac{\Delta N}{\Delta t}. \quad (3.1)$$

The pressure drop in the droplet phase is noted at roughly  $\Delta p = (14 \pm 3)$  psi  $\approx (1.0 \pm 0.2)$  bar. Hence, the total resistance computes to

$$R_{\text{chip}} = \frac{\Delta p}{\Delta Q} \approx (8.52 \pm 1.84) \cdot 10^{19} \frac{\text{kg}}{\text{m}^4 \text{s}}. \quad (3.2)$$

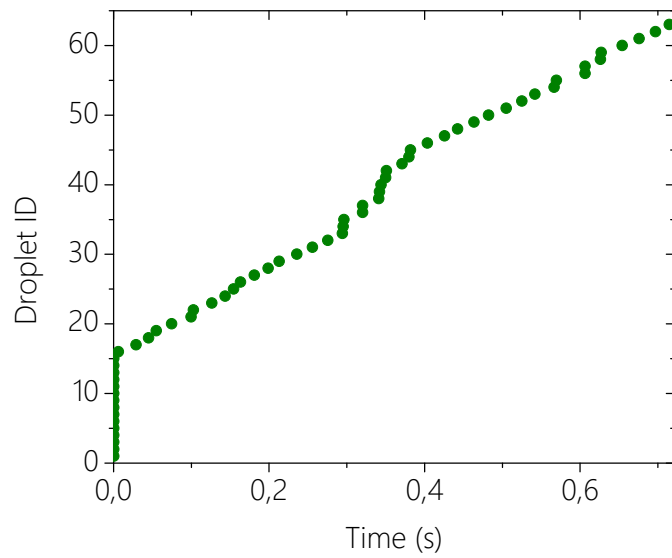


Figure 3.19: Detected droplets behind the flow-focusing regime yielding a generation rate of 66.5 droplets per second.



## Chapter 4

# Stabilization and characterization of mesoscopic droplet dispersions

Forming emulsions, either by simple blending of two immiscible liquids or, more advanced, using microfluidic chips, is just the first step in creating an adequate model system. To stabilize these dispersions, a closer look into the phase composition and its free-energy preferences is necessary. Picking a common example: foam, basically air bubbles in a liquid medium, is a very unstable model system. Despite all efforts of beer brewers, the air bubbles on a freshly tapped drink usually collapse within seconds or a few minutes [Rudin, 1957]. Coming back to microscopic dispersions with tailored properties, one is interested in interactions between droplets or particles. Moreover, the question arises whether droplets can after all serve as a model system like colloidal suspensions. Accordingly, this chapter examines dispersity, dynamics and dense configuration properties of microfluidically generated droplet emulsions.

## 4.1 Composing stable micro-droplet emulsions

Referring to the International Union of Pure and Applied Chemistry (IUPAC), "micro-emulsions are dispersions made of water, oil, and surfactant(s) and are isotropic as well as thermodynamically stable systems with dispersed domain diameter varying approximately from 1 to 100 nm, usually 10 to 50 nm" [Slomkowski, 2011]. Furthermore, it says that the average diameter of droplets in macro-emulsion (usually referred to as an emulsion) is close to one millimeter (i.e.,  $10^{-3}$  m). To be precise, emulsions containing droplets of 1 to 10 micrometers could be considered as meso-emulsions since their size range appears to be between the one of macro- and micro-emulsions [Maqsood A. Malik and Hashim, 2010].

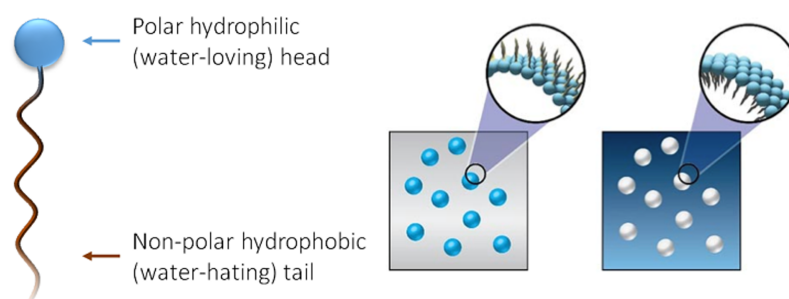


Figure 4.1: Assembly of surfactant molecules in formed micro-emulsions.

Depending on the dominant phase, hydrophilic as well as hydrophobic fluids can act as a continuous medium. In the experiments that contribute to this thesis, a fluorophilic oil is used as a continuous phase while different water compositions form the dispersed phase. Although both configurations are possible, an aqueous droplet phase's properties can be tuned more easily. Thus, it is aimed for to study their potential to experimentally act as colloidal particles with adjustable properties.

### 4.1.1 Dispersed droplet phase

The dispersed phase, also considered as droplet phase, has to be a polar solution due to the need of hydrophilic properties. To avoid electric charges that could yield adhesion effects, deionized water (di-water) is used for generic droplet generation. For biological applications, the use of buffer solutions (Phosphate-buffered saline, abbreviated PBS) is common as well.

	density [g/cm <sup>3</sup> ]	refractive index	dynamic viscosity [cP]
HFE-oil 7500	1.61	1.29	1.24
deionized water	1.00	1.33	1.01
60% sucrose	1.29	1.44	56.7
glycerol	1.26	1.47	1.41

Table 4.1: Relevant properties of the continuous fluorinated oil phase and polar dispersed phase solvents.

In this work, light interactions are intended to be induced. Thus, sucrose is added to di-water in the dispersed phase to increase the refractive index of the solution (see Chapter 5.2).

For applications requiring high refractive index, ethylene glycol has been tested against sucrose. Table 4.1.1 contrasts the properties of commonly utilized solvents in microfluidics. Sucrose and glycerol feature the largest refractive index compared to the oil carrier phase. Contrary to the ethylene alcohol, sucrose droplets show better stability in experiments. High viscosities of the dispersed medium yield a smaller diffusion coefficient within the droplet and towards its critical interface. Duly, it is suspected that this improves stability and prevents unwanted coalescence of micro-droplets. The sugar in the aqueous phase therefore acts as a stabilizing agent, as well as an optical manipulation promoter. Unless annotated differently, when referring to the term sucrose further in this thesis a mixture of 60% sucrose and 40% water is implied.

#### 4.1.2 Continuous carrier phase

Every experiment is performed using 3M Novec HFE-7500 (Hexane, 3-ethoxy-dodecafluoro-2-(trifluoromethyl), purity > 99%) as continuous oil phase. Novec HFE-7500 is a fluorocarbon oil with excellent properties for various microfluidic applications. It does not burn and has no electric conductivity. In industry, HFE broadly appears in heat conduction applications due to its high thermal stability [Electronics Markets Materials Division, 2009].

For optimal stability results on generated micro-droplets, an oil-soluble surface-active-agent is added to the continuous phase. Inclusion of 1% (by volume) of neat RAN 008-fluorosurfactant into HFE-oil establishes stability for droplet transfer in an external cell (Ibidi  $\mu$ -slide) and storage over weeks. Further details are carried out in the following subsection.

### 4.1.3 Gibbs free energy stabilization

Surfactant molecules settle at the interface between the droplet and the surrounding phase and therefore have emulsifying properties. Figure 4.1<sup>1</sup> illustrates the shape of a surfactant molecule with its polar head and its non-polar tail (left). The right part of Fig. 4.1 shows how these molecules arrange in a two-phase liquid system. Depending on whether the hydrophobic phase forms as a dispersed or continuous medium, the oil-dissolved fluoro-surfactant molecule orients its non-polar tail correspondingly.

To describe energy processes related to conformational changes in emulsions more precisely, the Gibbs-Duhem Equation (Eq. 4.1) is recalled. It shows that a system's surface free energy  $G$  is a sum of three components: the droplet's surface area  $A$  times their tension, conformational entropy  $S$  scaling with the temperature  $T$  and the emulsion composition with chemical potential  $\mu_i$  of each molecule  $i$ .

$$G = A\gamma - SdT + \sum_i n_i d\mu_i. \quad (4.1)$$

Thus, at a constant temperature and composition, interface/surface tension  $\gamma$  can be defined by deriving

$$\gamma = \left( \frac{\partial G}{\partial A} \right)_{T, n_i}. \quad (4.2)$$

Chapter 2.1 lists different ways emulsion breakdown occurs. Here, Fig. 4.2<sup>2</sup> contrasts formation and breakdown at energies  $G^I$  and  $G^{II}$ . One effect promoting droplet coalescence is flocculation. The process drives droplets closely together due to interfacial adhesion. Hence, clusters are formed and droplets lose spherical particle properties. The mechanism can be a precursor to coalescence that yields droplets to merge and fuse to larger ones.

In trying to understand conformational changes of a well-defined dispersed system, one can look at Gibbs free energy (Eq. 4.3). According to the second law of thermodynamics, a system's entropy  $S$  strives towards a maximum in order to reach equilibrium. The aim is to keep a sufficiently large droplet area  $A$  (scales with their radius squared) in stable condition. Provided the temperature  $T$  of the system is easily controlled at a constant level, the critical

---

<sup>1</sup>Figure by [University of Bristol, School of Chemistry, 2017].

<sup>2</sup>Image by [Tadros, 2013].

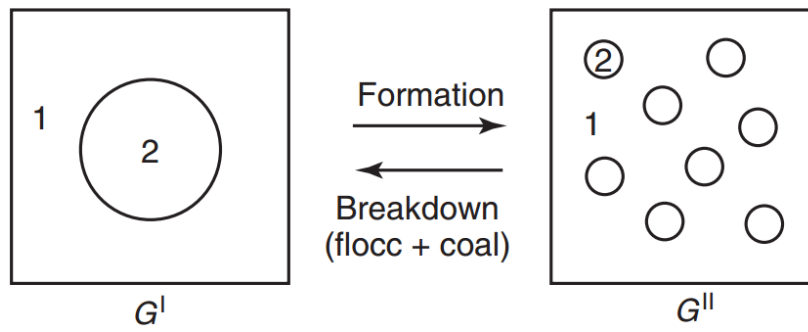


Figure 4.2: Potential  $G^I$  implies a phase-separated system,  $G^{II}$  a dispersed system.

value to balance is the droplet's interfacial tension  $\gamma$ .

$$\Delta G = \Delta A\gamma - T\Delta S \quad (4.3)$$

Figure 4.3 shows the free energy pathways. State  $G^{II}$  represents the lower energy level of a dispersed system and  $G^I$  the level of a phase-separated system. The breakdown due to incompatible or non-present surfactant is visualized by the red line. Adding a suitable stabilizer can create an energy barrier preventing coalescence as the green path's energy valley as  $G^V$  shows. A stabilizing agent such as surfactants or certain polymers can enable a kinetically stable system (state V), so that the process from state II to I becomes non-continuous.

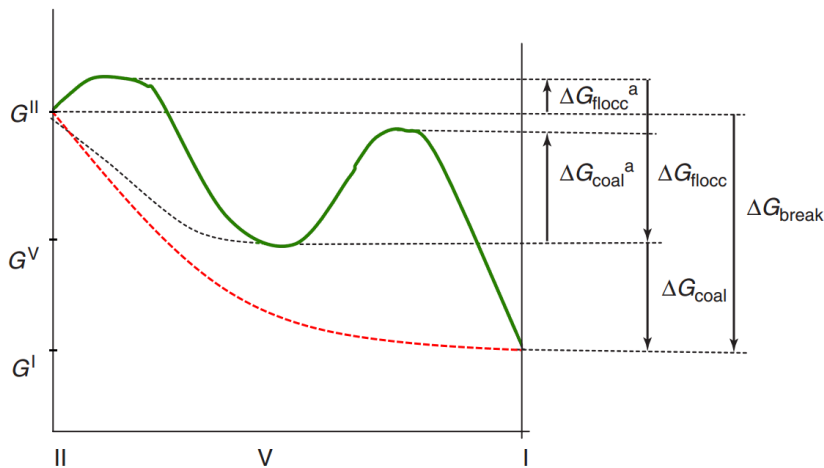


Figure 4.3: The Gibbs free energy path. Transition lines correspond to the presence (green) and the non-presence (red) of surfactant molecules.

Thus, the addition of a surface-active-agent to at least one inlet phase is conducive to the formation of droplets and essential to get a stability for longer than a couple of seconds time.

In the course of this work, four surfactants soluble in fluorinated oil and three dissolved in water were tested on their ability to improve controlled formation and lasting confirmation of droplets.

Experiments with 2% volume fraction of Brij 30, Hellmanex III and sodium dodecyl sulfate (SDS) surfactants that were added to deionized water showed no improved droplet stability. In fact, all of these tested surfactants composed to the aqueous phase prove inferior to oil-soluble surfactant. Hereafter, three different fluorosurfactants at certain concentrations were tried. Fluorosurfactants FC-4430, FC-4432 and FC-4434 were provided from 3M. From these three candidates, FC-4434 solely solved well in HFE and it was possible to form more durable droplets than with any of the water-soluble surfactants. However, droplets remain stable for minutes right after generation, but coalescence occurs before the transfer into external vials via polyethylene tubing is achieved.

Finally, a fourth surfactant is considered: non-ionic 008-Fluorosurfactant from RAN Biotechnologies. Thereupon, emulsion stability increases dramatically. At a 1% volume fraction dissolved in HFE, fluorosurfactant emulsions generated in previously presented PDMS chips can be relocated into an external sample cell. Properly sealed (HFE-oil evaporates at a rate similar to the one of water), mesoscopic droplet probes showed no noticeable aging effects in a 28 day period. The general structure of RAN 008 is perfluoropolyether-polyethylene glycol copolymer. However, the major difference is that 008-Fluorosurfactant is fluorosoluble while FC-4434 partly dissolves in water as well. Furthermore, FC4434 is pre-mixed with dipropylene glycol mono-methyl ether, which seems to affect droplet stability in a negative way. RAN 008 is not premixed with solvents and is supplied in its neat form to be dissolved solely in a fluorous solvent. Surfactant compatibility is a not yet well understood phenomena in physical chemistry. Further stability studies might potentially be very interesting. There are techniques such as light scattering, rheology and focus beam reflectance measurements to gain deeper insight.

Moreover, some concentration-related effects were investigated: surfactant fractions above the critical-micelle-concentration (CMC) lead micelle formation of surfactant molecules. This saturation yields to aggregation of droplets [Rosen, 2004]. Thus, in our experiments surfactant fractions of greater than 1% are relinquished to not induce particle coagulation. Furthermore, this value proved to create aqueous droplets in fluorinated oil that best match colloidal particle characteristics. At higher concentrations Brownian dynamics is hindered by strong interaction between droplets. Lower surfactant fractions decreased emulsion stability.

However, 008-fluorosurfactant has already been commercialized due to its reliable properties and is widely used in the microfluidic community.

#### 4.1.4 Creaming and sedimentation

Depending on the densities of a two-phase emulsion's inner and outer phases, dispersed droplets tend to sink to the bottom, cream on the surface or float. Here, a positive difference  $\Delta\rho = \Delta\rho_{\text{Droplet}} - \Delta\rho_{\text{Continuous}}$  yields sinking. However, according to Fig. 4.1.1, fluorinated oil has quite a large density compared to most aqueous solutions, so in most compositions creaming is likely.

The hydrodynamic force (or Stokes drag, Eq. 4.4) only depends on the composition of the continuous medium, which is fluorinated oil in this case. For particles in equilibrium the force is zero since it is directly proportional to the sedimentation/creaming velocity.

$$F_S = -6\pi\eta Rv_0. \quad (4.4)$$

In contrast, the gravitational force (Eq. 4.5) scales with the droplet's weight, which is determined by its volume and the phases'  $\Delta\rho$ .

$$F_G = \Delta mg = \left(\frac{4}{3}R^3\Delta\rho\right)g. \quad (4.5)$$

By equating both forces, the resulting creaming or sedimentation velocity reads

$$v_0 = \frac{2\Delta\rho g R^2}{9\eta}. \quad (4.6)$$

Table 4.1.4 states how long equilibration of formed droplet emulsions in an external sample cell might take. Water and sucrose droplets in oil settle at the cell's top (negative velocity) in 2 minutes at the most. Yet, the calculated sedimentation of comparable polystyrene particles in water takes 17 minutes, since their  $v_0$  is an order of magnitude smaller due to the low difference in density compared to the carrier medium water.

particle phase	$\Delta\rho$ [ $\text{g cm}^{-3}$ ]	$v_0$ [ $\mu\text{m s}^{-1}$ ]	equilibration time [s]
water	-0.61	-2.12	66.2
sucrose	-0.32	-1.13	124
polystyrene*	0.04	0.14	1016

Table 4.2: Sedimentation rates for aqueous droplets of radius  $1.4 \mu\text{m}$  in HFE-oil ( $\rho_o = 1.61 \text{ g cm}^{-3}$ ) stored within a cell of height  $0.14 \text{ mm}$  (Ibidi). \*Polystyrene particles dispersed in water ( $\rho_w = 1.00 \text{ g cm}^{-3}$ ) instead of oil.

The lower limit of the characteristic length scale  $l$  for Brownian motion to take place is about  $1 \text{ nm}$ . Thus, a typical ( $r = 1.4 \mu\text{m}$ ) sucrose droplet's gravitational potential  $F_G l$  computes to  $0.04 \text{ pN nm}$ . This confirms that the molecular diffusion potential dominates with  $k_B T$  being  $4.0 \text{ pN nm}$  at room temperature ( $20 \text{ }^\circ\text{C}$ ) and droplets are subject so thermal motion.

Thus, droplet emulsions make a model system for colloidal systems where creaming particles are needed. As Eq. 4.4 implies, creaming velocity is proportional to the force pushing particles towards the cell walls. Since the velocity is larger for droplets than for particles, droplet/wall interactions might become more relevant when looking at droplet emulsions rather than at polystyrene particle suspensions. Regarding laser tweezers, another circumstance deserves attention: subject to the set-up's design, a laser beam reaches the sample either from the top or from the bottom. Radiation pressure (see Sec. 5.1) pushes interacting objects along the optical axis. Depending on whether particles sit at the bottom or at the top of a sample cell, dynamics can increase or decrease under laser exposure.

## 4.2 Colloidal systems

Colloidal suspensions are well-investigated systems that play a large role in science, e.g. in soft matter physics and statistical mechanics. However, droplet microfluidics represents a novel development and brings interesting new perspectives to these fields.

Accordingly, there is rising interest in how droplet meso-emulsions differ from, or confirm with, colloidal systems. Especially experiments that involve particle flows are much easier conducted using a droplet generating chip, that produces the demanded objects already dispersed in solution. Flow speed, particle concentration and size dispersity are easily tunable via droplet systems that feature similar properties as colloidal systems.

### 4.2.1 Brownian motion

Molecules in the continuous phase (be it oil or water) thermally fluctuate at the default lab temperature (20 °C or 293 K) where all experiments are conducted. Thus, colloidal particles are subject to frequent collisions with surrounding liquid molecules. Because the particles are exposed to momentum from all directions in space, there is a continuous random displacement visible over time. This dynamics is called Brownian motion (R. Brown, 1827). However, the mean particle position  $\langle r(t) \rangle$  statistically remains zero since displacements along the positive and negative axes of travel cancel each other out. Nonetheless, the mean-squared displacement  $\langle r^2 \rangle$ , commonly referred to as MSD, grows with time. The substantial constant defining the speed of a particle exploring its surrounding area is the Diffusion constant  $D$ . In a simple two-dimensional environment (such as in sedimented or creamed (dilute) dispersions) Brownian dynamics are fully described with

$$\langle r(t)^2 \rangle = 4Dt. \quad (4.7)$$

The scaling constant  $D$  is characteristic for each particle size and depends on the surrounding phase's dynamic viscosity  $\eta$  and the ambient temperature  $T$ . According to Stokes-Einstein, the prediction for a droplet's (area-)velocity without external constraints is given by the diffusion coefficient

$$D = \frac{kT}{6\pi\eta R}. \quad (4.8)$$

### 4.2.2 Anomalous diffusion

In reality, diffusion rarely takes place without external influences. Thus, the MSD becomes proportional to time featuring an exponent  $\mu$  (Eq. 4.9). For the previously discussed case,  $\mu$  is 1, but it can take values smaller and larger than that.

$$\langle r(t)^2 \rangle \propto t^\mu. \quad (4.9)$$

Both the diffusion coefficient  $D$  and the anomalous exponent  $\mu$  can vary with time. To collect information about the constraint, time dependence of  $D(t)$  and  $\mu(t)$  for two-dimensional diffusion is examined.

$$D(t) = \frac{1}{4} \frac{\partial \langle r(t)^2 \rangle}{\partial t}. \quad (4.10)$$

$$\mu(t) = \frac{\partial \log \langle r(t)^2 \rangle}{\partial \log t}. \quad (4.11)$$

Figure 4.4<sup>3</sup> demonstrates the MSD over time dependence from the anomalous exponent  $\mu$ . If  $\mu$  becomes larger than 1 there is super-diffusion, and for values smaller than 1 it is sub-diffusion. Additional drifts or ambient vibrations can increase particle motion so super-diffusion is noted as visualized by the red line in Fig. 4.4. When geometrical constraints are present, laser traps or wall/particle interactions cause less growth in the MSD over time, called sub-diffusion (green line). The curve's shapes can give an idea of what interactions are involved in the anomalous behavior of droplet movement.

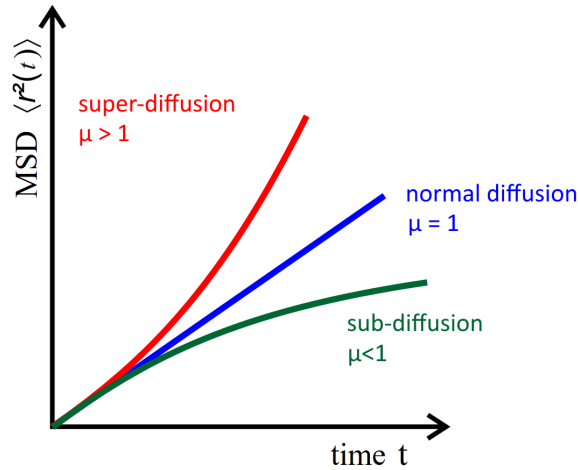


Figure 4.4: An exemplary MSD versus time plot according to Eq. 4.9. Each line corresponds to a value of  $\mu$  around 1.

---

<sup>3</sup>Figure by [Creative Commons Attribution-Share Alike 3.0 Unported, 2012]

## 4.3 Characterization of microfluidically designed emulsions

Figure 4.5 shows a photo of a typical external sample cell under the microscope. From a microfluidic chip's outlet, a thin (inner diameter 0.38mm) polyethylene tube allows transfer of generated droplet emulsions. This cell features three different outlets and yields the potential for droplet sorting. Before experiments are conducted that do not require flows, all three outlets are sealed to avoid evaporation after the channels are filled up. At a fraction of 1% RAN surfactant, droplet dispersions remain stable for an investigated time of at least a month inside this cell. An advantage of emulsions is that they can be generated in certain polydispersities or completely uniform. Thus, in the following section a sample featuring a wide size distribution is characterized.

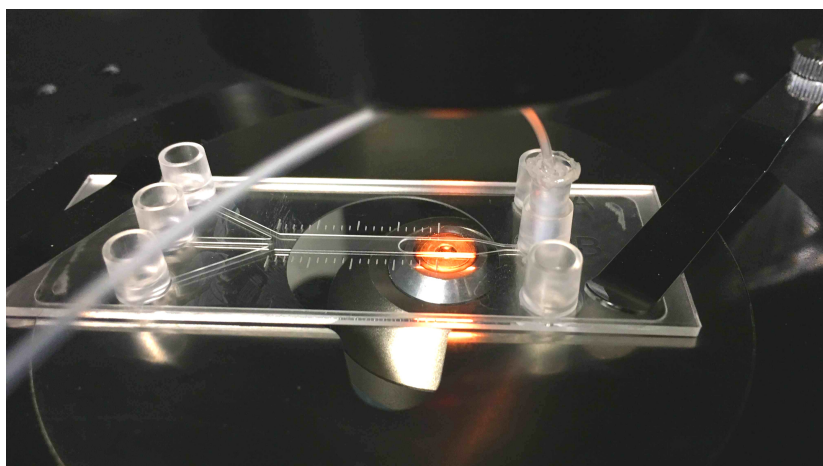


Figure 4.5: Droplet emulsion transfer into a sample cell (Ibidi Y-Cell) for further investigation.

### 4.3.1 Polydispersity in stored probes

The right image in Fig. 4.3.1 demonstrates a colloidal system made of droplets with increased polydispersity. By inlet pressure adjustment on the generation chip, different jetting regimes yield various droplet sizes. It was already shown that uniform emulsions with low size deviation ( $< 3\%$ ) can easily be formed using a PDMS chip (see Chapter 3) as well, but sometimes a certain particle size distribution is appreciated. Figure 4.3.1 contrasts a binary

particle suspension (left) with a polydisperse droplet emulsion (right). Both show Brownian motion.

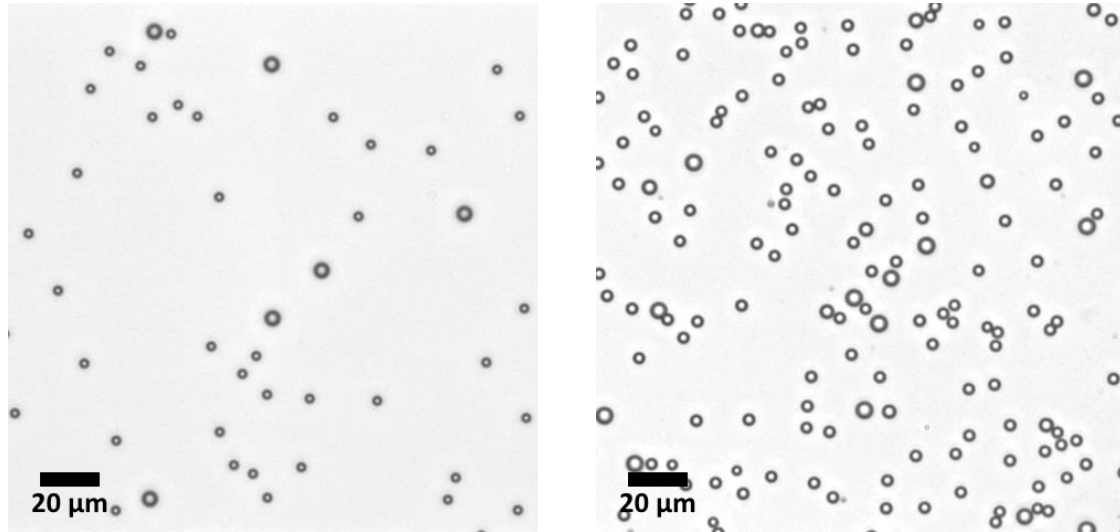


Figure 4.6: A binary polystyrene particle dispersion (left, 43 colloids) in contrast to a generated dilute and polydisperse emulsion (right, 145 droplets).

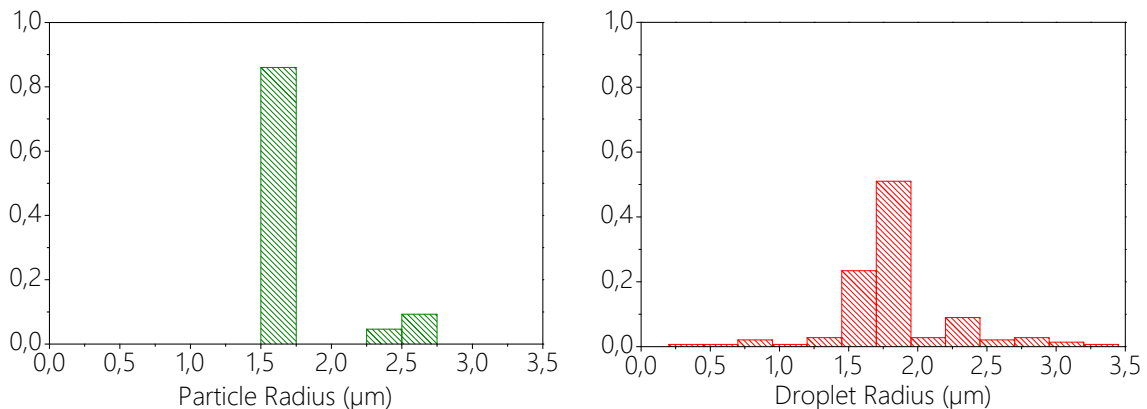


Figure 4.7: The normalized size histograms of the above probes. The binary particle dispersion (green) consists of 1.4μm and 2.5μm colloids. The droplet emulsion's mean diameter is 1.81μm with a standard deviation of 0.42μm (red).

Figure 4.3.1 shows size histograms for both dispersions from the images in Fig. 4.3.1 above. The right (red) figure corresponds to its image of the droplets dispersion above and shows the induced polydispersity with a mean radius of 1.81 μm in radius. However, there is a small fraction of droplets larger than 2 μm. Since these bigger droplets range in a different size regime, they are treated separately in the following to have a comparison in diffusion dynamics. Regarding the binary colloidal suspension on the left in Fig. 4.3.1, it is known for a

fact that its colloids have a very uniform radius of 1.4 and 2.5  $\mu\text{m}$  (commercially sold as such, low standard deviation in size). Nonetheless, greyscale image particle detection narrowly overestimates their sizes. This systematical error is due to the dark edges around objects on bright-field microscope images. The margin's contribution to the overall radius of larger particles is lower, so the error vanishes. However, further investigation with confocal imaging methods using oil objectives or light scattering, promising better accuracy, are possible.

#### 4.3.2 Droplet and particle dynamics

Earlier, Brownian motion was introduced. Provided that electric charges and wall interactions can be neglected, aqueous droplets should be able to perform normal ( $\mu = 1$ ) two-dimensional diffusion within an oil medium. In the following section, the difference in diffusion of colloidal particles and droplets is being studied. Using an IDL-software environment, particle positions are tracked [Crocker and Grier, 1996]. Data is collected at an acquisition rate of 10 fps over 50.000 images. Overall experimental time for each curve is 5000 seconds (approximately 1.5 hours). By recording the particles' displacements between the frames, their trajectories can then be captured. Each data point is averaged over the whole ensemble of droplets. Additionally, trajectory times are measured in time intervals rather than on the absolute timescale. Thus, very good statistics are achieved for short time spans. For long time intervals, there are just few trajectories  $N$  to average over. Accordingly, the accuracy of presented data decreases exceedingly with time.

The red curve in Fig. 4.8 plots the droplet's mean-squared-displacement over time. As mentioned, just droplets smaller than 2  $\mu\text{m}$  in radius from Fig. 4.3.1 are tracked. Additionally, three different sizes of diluted polystyrene particle suspensions (area fraction about 1%) in water are considered for comparison (green, blue and cyan lines). Taking a look at the curve's overall shapes, the expected linear dependence between displacement and time for normal diffusion is noticed. Beware that both scales are logarithmic, so within one plot one is able to detect small changes in the short time range, as well as large displacements in the long range. There are colloids diffusing faster (2.5  $\mu\text{m}$  and 2.9  $\mu\text{m}$ ) than the droplets (red line), and there are slower (larger) particles (4.2  $\mu\text{m}$ ). However, contrary to the colloids, a decreased slope at intermediate times is visible in the droplet curve. The behavior does not seem to affect short term diffusion, but induces superdiffusion in long time ranges.

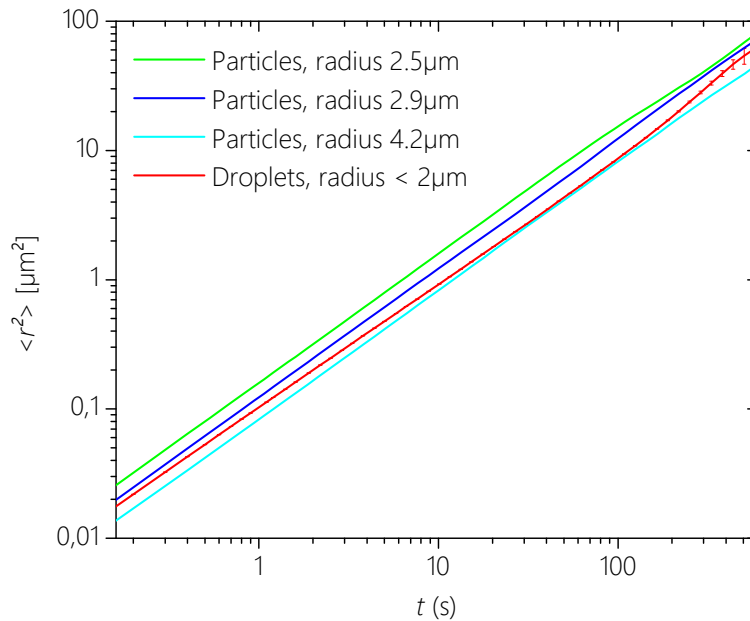


Figure 4.8: Comparison of polystyrene particle's and sucrose droplet's MSD over time on a logarithmic scale. Error bars to the droplet's curve are representatively plotted.

For closer investigation of the lines' slopes, Fig. 4.9 plots the time corresponding diffusion coefficients over time. Within the first second already, the droplet's diffusion rate drops down to the one of the 4.1  $\mu\text{m}$  particles. Yet, the rate seems to recover for diffusion trajectories longer than 200 s, although long times statistics are not sufficiently accurate to justify concrete claims. The corresponding error bars are plotted in Fig. 4.8 and Fig. 4.9 only for the droplet's data but can be regarded representatively.

Reviewing a time-lapse series of the acquired microscope images from the experiment gives a hint of where the slowdown might be originated. Droplets, that cross their paths and closely approach, dance around each other for some time before they let go. It is suspected that the effect comes from the short range Van der Waals interaction induced by the surfactant layer on the droplet interface. For short diffusion times, droplets seldom meet and diffuse freely, for intermediate times they are affected from the surfactant adhesion between each other, and for very long times they (on average) have already been able to detach. However, in future experiments, modified sample compositions might be able to create an electrostatic repulsion, which can help minimize this effect.

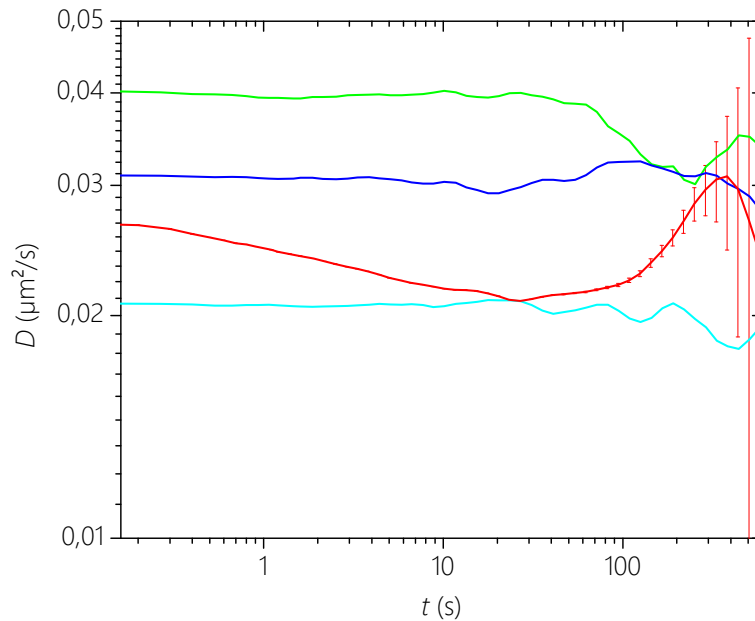


Figure 4.9: The droplet's diffusion coefficient (red line) shows a decrease for intermediate times while particle diffusion stays constant (disregarding long time effects).

Especially droplet short time diffusion ( $< 1$  s) tells about its characteristic properties since it has not been able to explore any surroundings so far. More data from polystyrene particles, acquired in a previous project, allows to bring droplet data in cohesion. Figure 4.10 displays the diffusion coefficients for various polystyrene particles between  $0.8 \mu\text{m}$  and  $4.2 \mu\text{m}$  (green), and for the droplets in the probe studied here (red). Particle data is acquired under ideal conditions so  $D$  stays constant over the full time range (similar to Fig. 4.9). The dashed lines show theoretical predictions from Eq. 4.8 for the viscosity values of water (green) and fluorinated oil (red).

Aside from the expected difference between droplet and particle coefficients due to the viscosities of their surrounding medium, a systematically decreased diffusion rate compared to the theory is examined. However, this phenomena has already been investigated by Faxen in 1922. Thus, a particle mobility factor was introduced, that can be used to correct the theoretical value for diffusion close to cell-walls. Overall, a similar dynamics between droplet emulsions and particle dispersions is investigated. Especially when polydisperse probes are of interest, emulsions present an alternative to conventional colloidal suspensions.

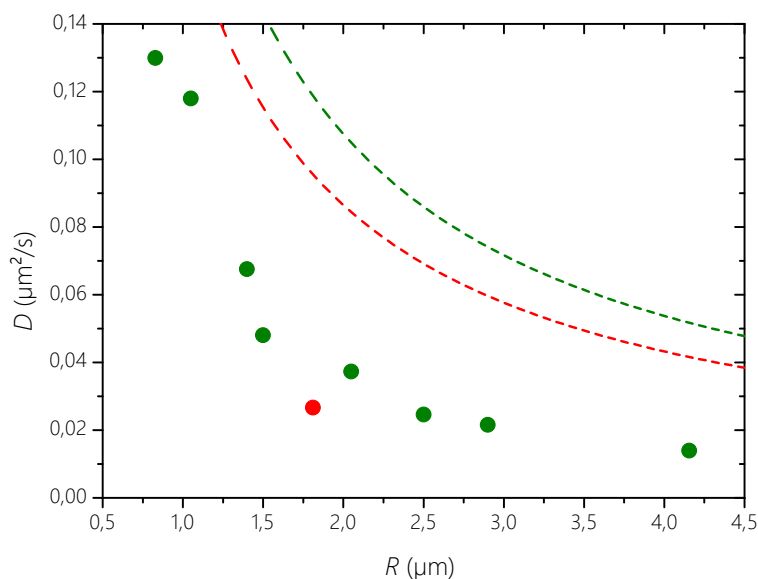


Figure 4.10: Measured diffusion coefficients (within the trajectory's first second) versus particle radius. Green dots refer to measured particles, the red dot to regarded droplets. Two dashed lines show theoretical predictions for diffusion in water (green) and oil (red) according to Stokes-Einstein.

### 4.3.3 Pair-distribution in very dense configurations

Although droplets might sometimes be characterized as soft sphere particles, the interfacial tension in femtoliter volume dimensions is large enough not to allow any visible shape deformation under flow conditions. Notwithstanding that, dense two-dimensional droplet populations can lead to high pressures so droplets might morph into hexagonal shapes. Hence, droplet emulsions cannot be seen as a classical hard-sphere model system [D. Grasso and Bergendahl, 2002]. Nevertheless, interesting crystallization effects occur during the work with mesoscopic droplets.

During an experiment, droplet formation is abruptly stopped by sealing the outlet so pressure in the collection chamber increases. Nonetheless, droplet generation continues for a short period and the chamber runs full with droplets of a low polydispersity. Figure 4.11 shows a hexagonal self-assembly of nearest neighbor droplets where crystal assembly is suspected. Accordingly, regular domains of monodisperse droplet crystallization are arranged. Borders between arranged aggregates appear. The sample was generated with 3% RAN fluorosurfac-

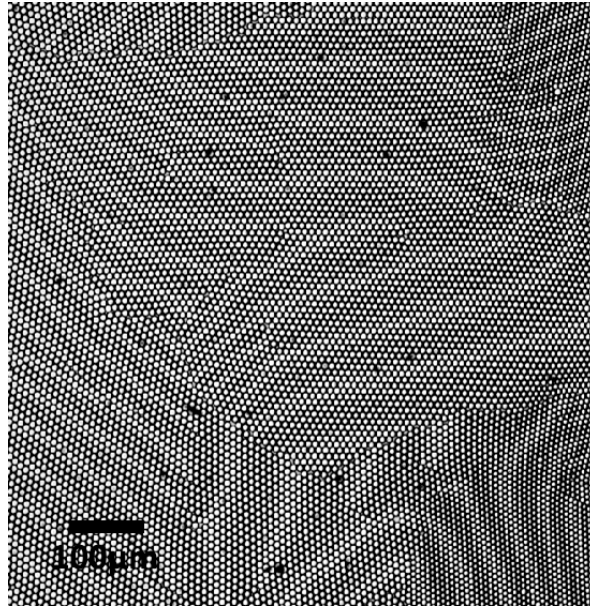


Figure 4.11: A dense droplet population with a high surfactant fraction in the collection area of the chip it was produced in.

tant, instead of the common 1% volume fraction. Due to the high surfactant concentration droplets aggregate and Brownian motion is not present.

For measuring the quality of crystallization the radial- or pair-distribution function of Fig. 4.11 is calculated. In general, the function  $g(r)$  demonstrates the number of droplets sitting in a distance  $r$  from the reference object at position 0. The reference is averaged over all tracked droplets. Additionally,  $g(r)$  is normalized, so that for an ideal gas the probability of finding a particle in distance  $r$  from the reference approaches 1. In contrast to an ideal gas, which claims to be the most random particle distribution, a colloidal crystal is well-organized. Thus, in a perfect two-dimensional crystal, it is most likely to detect the next-neighbor particle in the range of exactly one diameter.

Looking closely at Fig. 4.12, double-peaks in regular distances become apparent. This appearance is typical for a face-centered cubic system (fcc-lattice), which conform with the closest packing fraction for an area (two-dimensional crystal). Also, small spikes between the regular orders are noticed. However, these are due to a slight polydispersity in the given probe. In fact, the regularity in intensity of the first three orders yields an apparent crystal structure. Higher orders (in multiple radius range) vanish, although the first four peaks appear homogeneously. Collectively, a superposition of radial-distribution-functions is assumed, since the given image shows several crystalline domains that have been analyzed

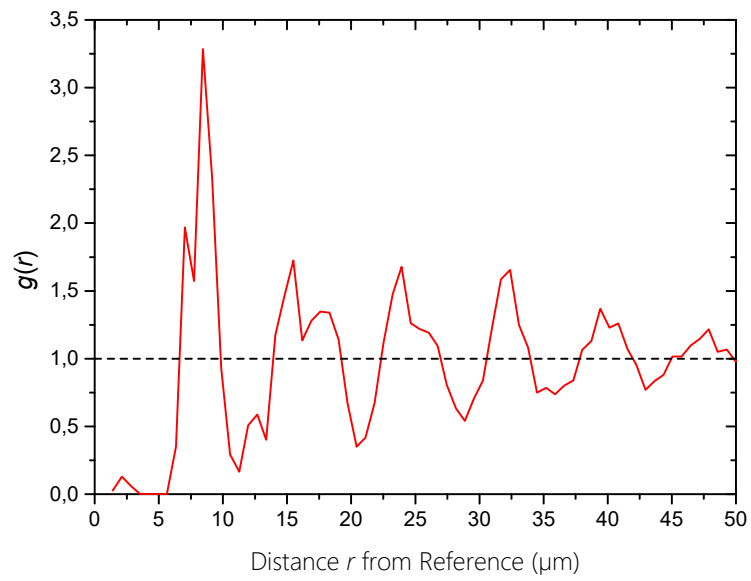


Figure 4.12: The pair-distribution-function  $g(r)$  of Fig. 4.11.

together.

## **Chapter 5**

# **Exposure of micro-droplets to laser potentials**

This chapter aims to investigate the influence of optical tweezers on small volume droplets with a tuned refractive index. The special focus lies on rough laser potentials, which are well studied regarding hard sphere dynamics but have never been considered in combination with droplet microfluidics. Hence, the effect on droplets performing Brownian motion is discussed to get an idea of how well previous experimental results can be translated from particle into droplet physics. Furthermore, for microfluidic on-chip-applications, it is of importance to assess whether tweezer forces are large enough to trap droplets from a stream right after generation. Therefore, laser potential effects are evaluated on flow configurations as well.

## 5.1 Forces exerted by optical tweezers

Optical traps use highly focused laser beams to apply forces on objects whose refractive index differs from the surrounding medium. The effective index of a particle is defined as the index of the particle  $n_2$  divided by the index of the surrounding medium  $n_1$ ; that is,  $n = n_2/n_1$ . A polystyrene sphere in water has  $n = 1.6/1.33 = 1.2$ .

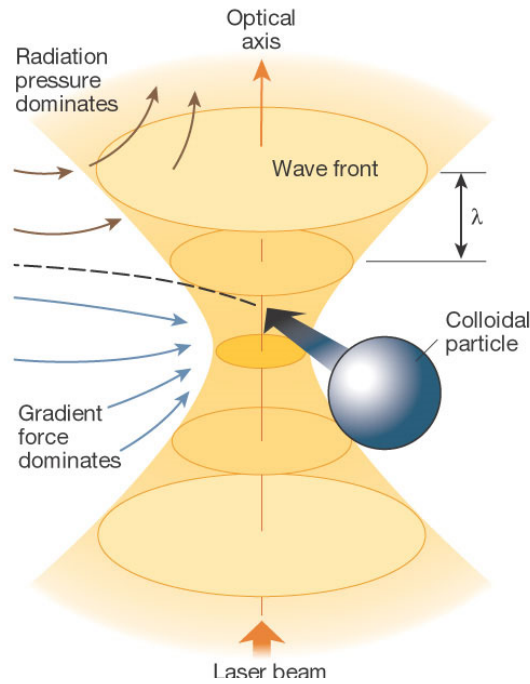


Figure 5.1: Optical tweezer forces consisting of radiation pressure and gradient force.

To get an estimate of the force focused laser beams are able to apply on particles in solution, one uses

$$F = Q \frac{nP}{c_0}. \quad (5.1)$$

The dimensionless quantity  $Q$  in Eq. 5.1 states the fraction of photons that effectively interact with the droplet and is estimated here at around 0.1 ( $Q$  depends on the perpendicular or parallel axis as well, see [Ashkin, 1992]). Since laser power and refractive index are of order 1, the exerted force scales with the speed of light's reciprocal value (order  $10^{-9}$ ), yielding an overall laser tweezer force in the piconewton regime.

Figure 5.1<sup>1</sup> illustrates the two forces involved in trapping colloidal particles (radius > laser wavelength). Here, the laser beam comes from the bottom of the image and travels along a perpendicular axis. On one hand, the scattering force drives the particle along the optical axis. On the other hand, a gradient force pulls it towards the highest laser intensity (the laser focus). Photons are deflected within the optically denser particle/droplet medium and thus transfer momentum. For calculations on each force's components see [Grier, 2003].

## 5.2 Refractive index adjustment of the dispersed phase

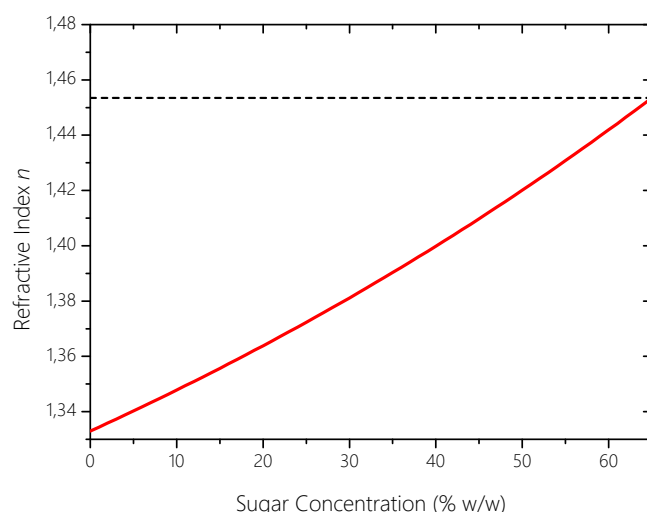


Figure 5.2: Refractive index of sucrose solutions at 20.0 °C and 589.29 nm wavelength.

In order to move a droplet with laser tweezers, the difference between refractive indexes of the dispersed and continuous phase must be maximized [Molloy and Padgett, 2002]. It is beneficial not to change the properties of established droplet phase compositions to preserve comparability with other microfluidics publications. Therefore, the refractive index of the aqueous phase is adjusted. Yet, the addition of sugar seems adequate to achieve an appropriate difference in refractive indexes to the one of HFE oil. HFE 7500 has a refractive index of 1.2870, slightly smaller than that of water with 1.3300 at room temperature. Figure 5.2<sup>2</sup> shows the refractive index dependence of deionized water as a function of its sucrose frac-

<sup>1</sup>Figure by [Grier, 2003].

<sup>2</sup>Data from [International Commission for Uniform Methods of Sugar Analysis, 1989]

tion. Nearly saturating deionized water with sucrose, the solution becomes applicable for optical tweezer use, e.g. a 65% sugar fraction (with 35% water in the final solution) yields a refractive index of 1.4532.

### 5.3 Single beam trapping of droplets in a flow

To experimentally verify the amount of force  $F_T$  an optical tweezer can apply on refractive index tuned droplets, a simple approach is selected. A fixed optical trap (1,500 mW power) is directed on a stream of generated sucrose droplets. In normal operation (at around 10 psi inlet pressure), the chips ejects a dense flood of droplets much too fast to be trapped (in fact, a 1000 fps high-speed camera cannot even capture them). Lowering the inlet's phases' flowrates both slows down droplets and increases their nearest neighbor distance. Accordingly, the flow is adjusted, so droplets pass the tweezer spot one by one. Thus, the flowrate is decreased in small steps until velocity is sufficiently small for single droplets to be retained. By measuring the droplet's speed right before it is trapped, the Stokes forces  $F_S$  introduced in Chapter 4.1.4 can be evaluated and should be equal to the minimum optical tweezer force (see Eq. 5.2).

Figure 5.3 illustrates a droplet in a the channel flowing from left to right. As case a) shows, in an equilibrated flow condition the droplet flows with constant velocity since Stokes drag cancels out flow pressure of the continuous medium. In b) there is a laser tweezer applied on the droplet stream. When a laser tweezer's perpendicular force's component is equal to (or larger than) Stokes force, trapping is possible and the droplet reaches zero velocity. The Stokes drag, opposing the flow pressure forces that drive the droplet towards the chip's outlet, is proportional to the object's radius and the viscosity of its surrounding medium. Most importantly, Stokes drag scales with the velocity, so if a droplet moves with constant speed both forces match and can be calculated.

$$F_T \geq F_S = 6\pi\eta Rv_0 \quad (5.2)$$

To estimate the corresponding forces, video data (21,500 frames, 135 s) from the experiment is evaluated with help of DMV (see Sec. 3.4.3). Histograms of tweezed droplets' sizes

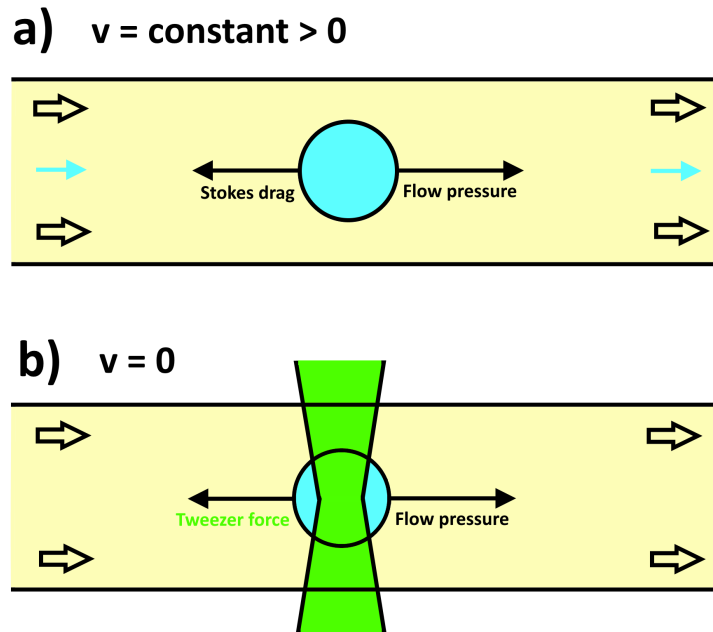


Figure 5.3: a) Droplet flow from left to right with constant velocity. b) Same flow with an applied laser trap that is just as strong to stop the droplet.

and velocities are presented in Fig. 5.4. By inserting these values, as well as the dynamic viscosity of fluorinated oil, a minimum tweezer force  $F_T = (31.9 \pm 4.7)$  pN is derived.

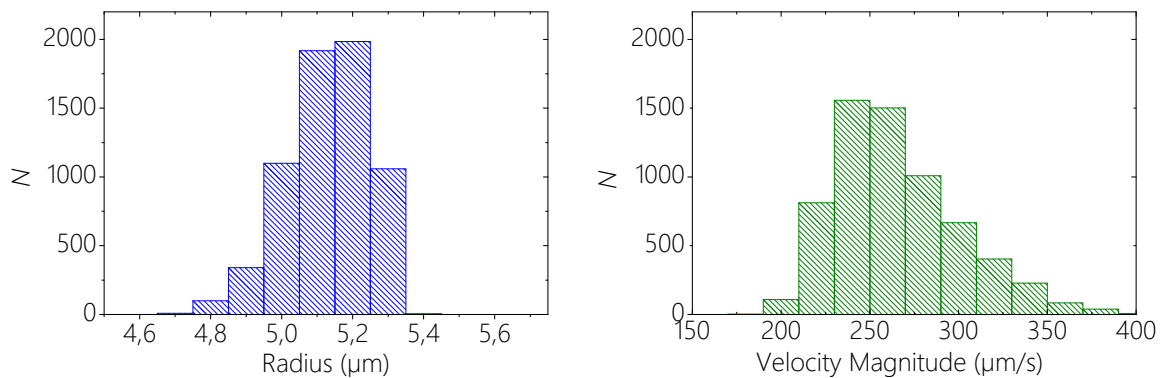


Figure 5.4: Properties of uniform droplets in a flow established at very low inlet pressures ( $\approx 1$  psi) slow enough for the optical tweezer to trap them. The mean radius is  $5.13 \mu\text{m}$  with a standard deviation of  $0.16$  ( $= 3.12\%$ ) and the velocity magnitude is  $(266.0 \pm 38.0) \mu\text{m/s}$  in the chip's manipulation domain.

The optical tweezer's forces match well with the order of magnitude that is predicted theoretically at the beginning of this chapter according to Eq. 5.1.

### 5.3.1 Estimation of the trap stiffness

Figure 5.5 shows a microscope image which is part of a captured video where a droplet flow is trapped. As visualized in Fig. 5.3, a droplet enters the field of view from the left and is trapped by the tweezer (bright spot). The trap's diameter measures exactly one droplet's dimension. When a new droplet chooses the same path and hits the tweezed companion directly, its momentum transfers and the trapped object is released.

With knowledge of the critical droplet velocity the tweezer can trap, it is possible to give an estimate of its spring constant  $\kappa$  (also called trap stiffness). If broken down to simple physics, one can assume that the trap's elastic potential fully decelerates the droplet and should therefore be equal to its kinetic energy. Accordingly, the particle diameter is assumed to be the trap's size  $s$ .

$$E_{\text{spring}} = E_{\text{kinetic}} \quad (5.3)$$

yields

$$\frac{1}{2}\kappa s^2 = \frac{1}{2}mv^2. \quad (5.4)$$

Thus, in the case of trapping a spherical object of the laser spot's size ( $s = 2r$ ) with velocity  $v_0$ , the tweezer's stiffness is

$$\kappa = \frac{mv^2}{s^2} = \frac{\pi}{3}\rho r v_0^2. \quad (5.5)$$

Hence, the optical tweezer's minimum spring constant computes to  $\kappa = (4.90 \pm 1.41) \cdot 10^{-10} \text{ kg s}^{-2}$ .

Certainly, this calculation just gives an approximation of the trap's properties (force and stiffness) and should not be used for quantitative comparisons, although it is sufficient to assess the order of magnitude. However, it is important to mention that the experiment generally underestimates the tweezer's actual force since not necessarily its whole amount is applied

to the trapped object. Furthermore, a more accurate adjustability of the flow pressure would allow to come closer to the critical trapping velocity. There are very precise methods to compute the optical tweezer's properties [Jong-Ho Baek and Lee, 2007] using thermal fluctuations or particle-step-response.

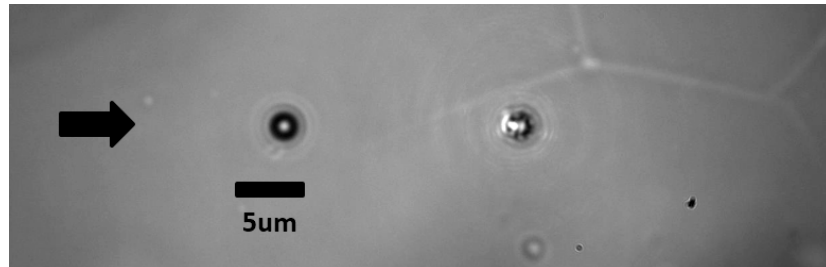


Figure 5.5: Microscope image of the trapping experiment. A droplet of  $5.13 \mu\text{m}$  radius enters the image from the left towards the trap on the right. One droplet is already tweezed.

## 5.4 Rough laser potentials

A rough laser potential can be seen as a combination of randomly distributed optical tweezers of different strengths, forming energy minimums and maximums. Thus, often it is referred to as random potential energy landscape (rPEL). Figure 5.6<sup>3</sup> shows a three-dimensional simulation of how a particle perceives the potential. The rPEL set-up used in this work (see Fig. 5.4) is designed so that the beam reaches a probe from the top. Usually, laser beams form a Gaussian-top with a strong intensity gradient towards the focus. In this set-up, a flat-top is established using a diffuser element so the light intensity spreads homogeneously over the captured sample area. To then generate an rPEL a green laser ( $\lambda = 512 \text{ nm}$ ) with 2,600mW maximum power (laser class 4) runs through an optical element that scatters light heterogeneously to create a superposition of optical traps.

### 5.4.1 Effect on dilute sucrose droplet emulsions

The commonly studied case of colloidal particles in laser potentials involves sedimented polystyrene particles. Here, the potential comes from the top. Thus, colloids feel the en-

<sup>3</sup>Image by [Florian Evers and Egelhaaf, 2013].

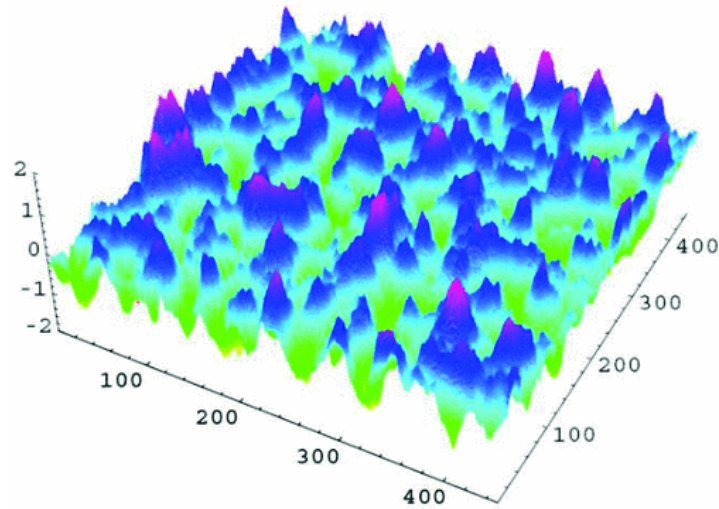


Figure 5.6: Spatially correlated Gaussian potential energy landscape. The x-y-plane corresponds to the spatial dimensions while the z-axis symbolizes laser intensity.

trapping of its distributed tweezers, as well as the radiation pressure that forces them further towards the cell's bottom. As a result, sub-diffusive dynamics dominate [Bewerunge and Egelhaaf, 2015]. However, the short time diffusion is mainly affected by increased wall interactions and for intermediate trajectory times, a sub-diffusion plateau is observed (in the MSD versus time plot) that is due to the particle's temporarily entrapment through potential minimums. In the long term, colloids overcome the trap's influence and return to normal diffusion ( $\mu = 1$ ). Yet, this has all been very well-studied regarding colloidal suspensions. So far, there are no studies on how droplets react to rough energy potential landscapes.

As mentioned in Sec. 4.1.4, sucrose droplets cream at the sample cell's top wall in equilibrium. Hence, radiation forces push creamed droplets away from the wall, rather than towards it. When applying high random laser forces over the whole droplet sample that is subject to Brownian dynamics, two outcomes are conceivable:

- a) Droplets, that were previously slowed down due to wall impacts, diffuse at a higher rate  $D$ .
- b) (Some) droplets perform sub-diffusion (exponent  $\mu < 1$ ) due to entrapment in distributed optical tweezers – just as expected from sedimented particles.

To get to the bottom of things, the droplet's mean-squared-displacement data is evaluated. To distinguish effects between large and small sizes, the polydisperse distribution from Fig. 4.3.2 is tracked for droplets of a radius lower or higher than two micrometers separately. Figure 5.7 shows the droplet dynamics of the previously discussed sample for different con-

figurations over time. The red and orange line originate from a free diffusion experiment, the green and blue curves represent the exact same droplets exposed to a rPEL at maximum power. Additionally, the diffusion coefficient's time-dependence plotted in Fig. 5.8 is closer inspected, as well as the exponent  $\mu(t)$  showed in Fig. 5.9.

The plot can be segmented into three domains:  $0 < t_0 < 1$  s,  $1$  s  $< t_1 < 100$  s and  $t_2 > 100$  s. Time-spans shorter than one second show short time diffusion. As expected in Sec. 4.3.2, larger droplets have a lower diffusion coefficient than their smaller companions. However, looking at the parameter  $\mu$  large droplets are already in a sub-diffusion regime. Interestingly, for both little and big droplets an increased diffusion rate  $D(t_0)$  is observed when laser forces are present. Since surface impacts prevail for short range diffusion, this supports theory a), indicating that laser pressure reduces the cell wall interactions of creaming droplets.

In the intermediate time regime  $t_1$ , it is clearly visible that dynamics for laser exposed droplets are confined (matching predicted theory b)). For both, droplets greater and smaller than  $2 \mu\text{m}$ , diffusion speed decreases. The time exponent  $\mu$  reaches its minimum at around  $t = 40$  s for small, a little earlier for large droplets. This is the so-called plateau-time, when, by average, most objects feel laser-trapped.

Corresponding to particles, in the time frame  $t_2$  droplets release themselves from optical tweezer potential peaks in the long term, so the value of  $\mu$  evolves towards 1 (where it stayed over the full range for non-laser-exposed diffusion). Again, beware that statistics are not precise for  $t_2$  (see error bars in previous chapter). However, contrary to the constant normal-diffusion rates, the coefficient for exposed droplets tends toward 0 for time-spans exceeding the plot's range.

The effect of a decreased diffusion rate due to surfactant adhesion of close droplets has been investigated in the previous chapter. After all, it does not play a major role ( $\Delta D \approx 6.0 \cdot 10^{-3} \mu\text{m}^2\text{s}^{-1}$ ) compared to laser influences ( $\Delta D \approx 2.5 \cdot 10^{-2} \mu\text{m}^2\text{s}^{-1}$ ). It can be concluded, that droplets behave very similar to particle dispersions in terms of Brownian dynamics and laser reaction. Both predicted effects a) and b) occur during our experiment. In fact, droplets give an interesting system for creaming dispersions.

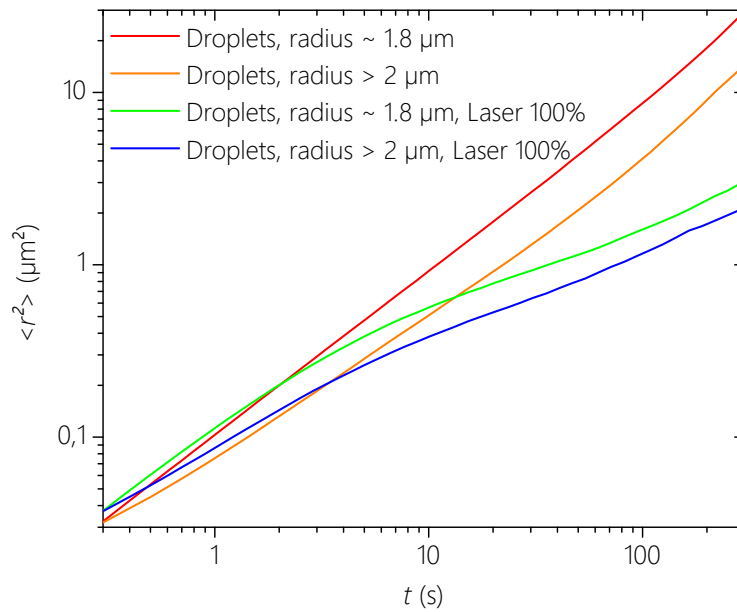


Figure 5.7: Droplet's mean-squared displacement over the time  $t$ .

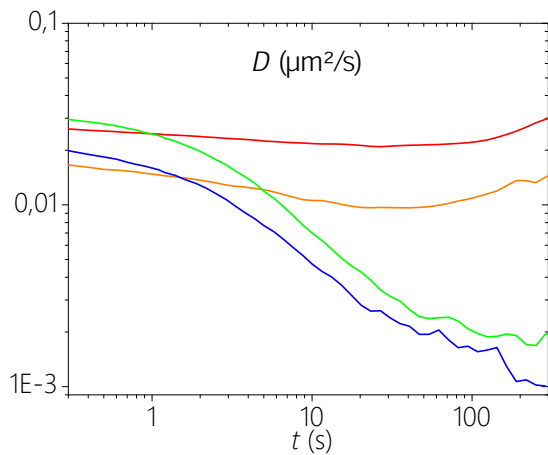


Figure 5.8: Diffusion coefficient versus  $t$ .

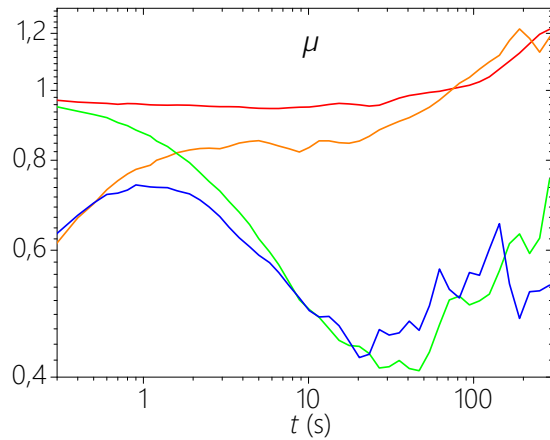


Figure 5.9: Exponent  $\mu$  versus  $t$ .

### 5.4.2 Different laser powers on dense droplet emulsions

For verification that the rPEL's radiation pressure pushes creamed droplets off the cell's top wall, a very dense population is investigated. Here, droplets feel the tight cage their surrounding objects form (see Fig. 5.10), so sub-diffusion must be present. Now, figuratively spoken,

the random potential landscape from Fig. 5.6 is laid onto the creaming probe. However, this might displace droplets sitting at places where intensity maximums occur. Other droplets, positioned in intensity valleys, are assumed to diffuse freely (although, with respect to the high droplet area fraction, still feeling a constraint) in two dimensions.

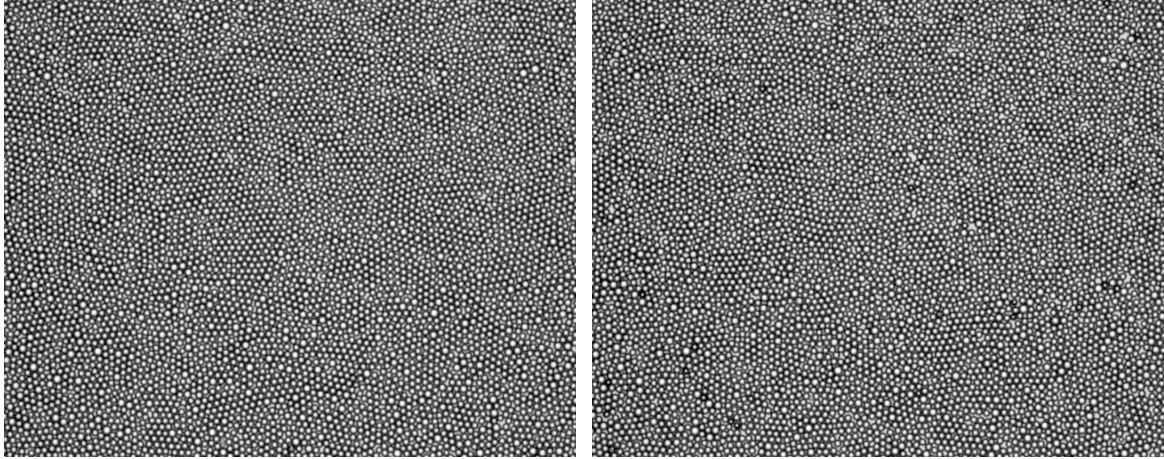


Figure 5.10: Dense population without field. Figure 5.11: Same sample with 100% rPEL.

Figure 5.10 and 5.11 show the dense droplet configuration without external field (left) and with a rPEL on full laser power (right). In the left image, the droplet area fraction is at a large value but Brownian motion is still present in just one 2d-layer. Hence, the black spots in the right image show droplets which are positioned under this layer, and therefore displaced into the third dimension. Over the course of our measurements (each 50,000 frames at 10 fps) the dark spots frequently appear at the exact same spots. Duly, they are suspected to map the rPEL's maximum force peaks. At these locations, laser tweezer radiation pressure pushes droplets in vertical direction. Droplet dynamics measurements are performed at 0 mW, 917 mW (80%), 1,640 mW (90%) and 2,600 mW (100%) laser power.

Figure 5.12 shows the MSD over time plot for the dense droplet population above exposed to four laser powers. The line colors from red to blue each symbolize applied rPEL intensities from low to high. As the graph demonstrates, there is no major difference in diffusion properties comparing 0%, 80% and 90% intensity. Figure 5.13 plots the diffusion coefficients corresponding to above MSD curves. Since the droplets from this dense probe are the very same ones that were studied in the previous chapter for the dilute case, it can be noted that  $D_{\text{short}} = D(t_0)$  is reduced by a factor of three from about  $0.03 \mu\text{m}^2 \text{s}^{-1}$  (dilute) to approximately  $0.009 \mu\text{m}^2 \text{s}^{-1}$  (dense). Hence, this effect can be attributed just due to the high area fraction. Unlike in dilute probes, 100% laser potential induces an increase in short

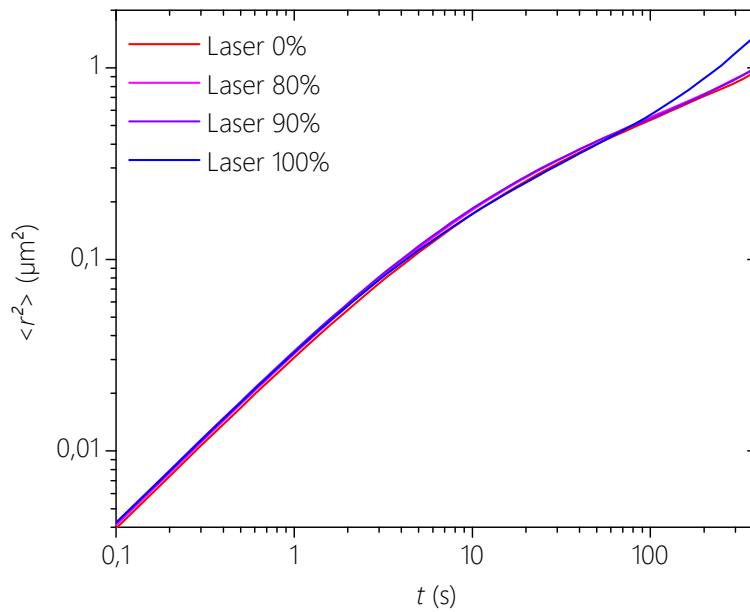


Figure 5.12: Droplet's mean-squared-displacement over the time  $t$ .

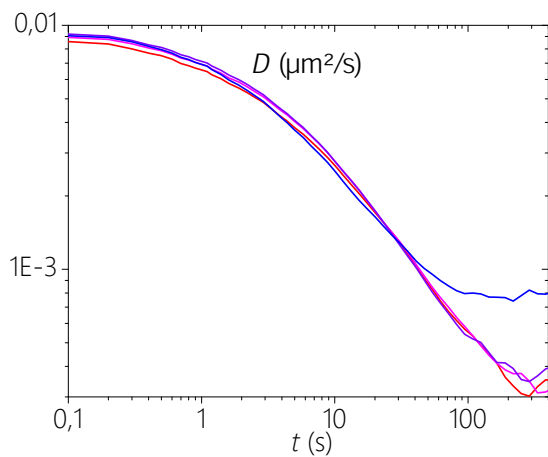


Figure 5.13: Diffusion rate  $D$  versus  $t$ .

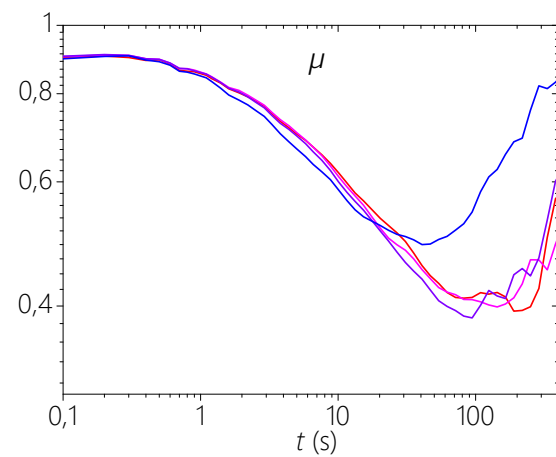


Figure 5.14: Anomaly parameter  $\mu$  versus  $t$ .

time diffusion, however, here is no difference evident.

As the associated anomalous exponent  $\mu$  versus time in Fig. 5.14 shows, a sizable distinction appears in the long term diffusion of caged droplets exposed to maximum laser power (blue line). For trajectory times larger than 10 s, these reach their sub-diffusion plateau earlier and somewhat less pronounced than their companions that are exposed to low laser intensi-

ties. In fact, these droplets even seem to recover towards normal diffusion when influenced by the rPEL. As the images imply, at 100% power droplets seem to get pushed out of the x-y plane (see Fig. 5.15). Thus, some explore the third dimension (the MSD then scales with  $6D(t)$  instead of  $4D(t)$ , see Eq. 4.7), while others have more free space for two-dimensional diffusion.

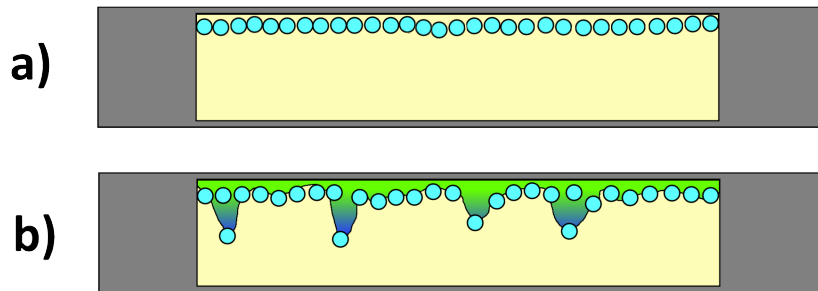


Figure 5.15: Sketch of a dense droplet probe in a sample cell (side view). No field is applied in a), while b) shows the same density probe with 100% rPEL.

Provided the optical axis runs opposite to the particles creaming/ sedimentation direction, a rPEL's radiation pressure definitely reduces wall/droplet interactions. Furthermore, it is able to visibly push droplets into another layer, so in dense populations it reduces sub-diffusion instead of promoting it. Figure 5.15 visualizes how an increased particle diffusion can be explained. In sketch a) no field is applied, while in b) the green/blue structure, which is laid on top of the sample, symbolizes an rPEL (compare with 5.6). Both cases a) and b) feature the exact same density of creamed droplets (30 objects). Due to the field induced displacement of single droplets into another layer, all objects have more space for diffusion and feel less constrained. Moreover, be it with or without rPEL power, one can generally claim that in dense configurations, droplet interactions are remarkably stronger than laser effects. The characteristic diffusion parameters  $\langle r^2 \rangle$  and  $D$  both fall about an order of magnitude below those of the previous section (dilute case).



# Chapter 6

## Conclusion and outlook

In this work, it is shown that two-phase droplet emulsions that can be produced within a microfluidic chip, are sufficiently small for optical tweezers to be applied upon and present a model system for Brownian motion equally-suited as that of colloidal dispersions. Tuned by refractive index using sucrose, these droplets obey laser tweezer manipulation.

On the way to an ideal emulsion, the physics of controlled droplet formation within microfluidics devices and how to design channel geometries according to the resistance's electric circuit analogy was elaborated. To be capable of generating uniform emulsions in the first place, a step-by-step demonstration of how to construct a microfluidic platform for on-demand droplet formation, was given. Not least, the phase composition plays a major role in order to avoid emulsion breakdown. Thus, 008-fluorosurfactant proved compatible with the continuous oil phase and confers an emulsion stability of at least a month.

Droplet and particle dynamics were compared using mean-squared-displacement, diffusion coefficient and the anomaly exponent. Hence, interesting surfactant effects for intermediate diffusion time-spans (contrasting droplets and generic colloids) were found. However, emulsions seems well-suited for experiments requiring a wider dispersity distribution than commercially sold dispersions. Moreover, a dense droplet population forming regular two-dimensional colloidal crystals was observed and characterized.

Rough energy potentials even offer the opportunity to apply a force field on droplet probes, constraining its particles' Brownian dynamics. However, one saw that the potential's radiation pressure increases the short time diffusion coefficient of creamed droplets since it pushes

them off the cell's top wall. Here, dense configuration interactions dominate over laser field induced effects. For future studies, droplet-droplet interactions and according surfactant influences need to be further considered, especially when generating higher density droplet probes. Laser potentials gave the possibility to tweeze freshly generated droplets from a stream in order to get an estimate of their trap's stiffness. Ultimately, the tweezer could be characterized even better by computation of its spring constant using the various droplet sizes the built chip is capable of producing.

Moreover, it is conceivable to swap the tubing on a microfluidic chip's inlet phases to generate oil droplets in sucrose, enabling a system whose outer medium's refractive index is larger than the one of its dispersed particles. Consequently, objects would then be repelled by optical forces.

An interesting application and further prospect of droplet microfluidics in combination with optical forces are microreactors. The tiny femtoliter volume droplets can be composed of any polar solvent. Thus, laser tweezers could induce micro-reaction by forcing droplets to coalesce. Though it is not yet included in this work, holographic laser tweezers are tested in the attempt of sorting droplets from a generated stream right within the microfluidic chip. Data on the efficiency of this process is a subject to be acquired at present.

---

# Acknowledgments

This work was only facilitated by the fertile collaboration between the Experimental Soft Matter Groups of Professor Egelhaaf from the Heinrich-Heine-University in Düsseldorf and Professor Weitz from the Harvard University in Cambridge, US-MA. I want to express my great gratitude to Stefan Egelhaaf for establishing the contact to David Weitz, for inspiring Skype discussions during my time abroad and for always having an open ear when I needed help in Düsseldorf. Especially, I would like to say thank you to David Weitz for funding the research, letting me use his lab facilities and always challenging me while at the same time providing constructive criticism. During my five months stay at Weitzlab, it was Kirk Mutafofpulos who introduced me to droplet microfluidics, helped me to set up my experiments and became a very good friend of mine. Also, I really appreciated the encouraging discussions I had with Manuel Escobedo, Dabasish Saha and many other colleagues from our team in Düsseldorf. Major thanks go to Florian Platten for reading over this work and contributing valuable observations that helped me a lot. Finally, I profoundly would like to thank Christoph Zunke who pragmatically supported my lab work, proofread the whole thesis with great perfectionism and gave valuable feedback every day and at literally any time.

The most important person backing this thesis has always been Laura who motivated me all along the way. She patiently reviewed each and every text line for me. Thank you so much for all of this.

Lastly, I thank Professor Axel Görlitz for being the second examiner of this work and the Hedwig and Waldemar Hort Stiftung for financially supporting the first three months of my stay in the United States.



# Bibliography

- [Adam R. Abate and Weitz, 2013] Adam R. Abate, Tony Hung, R. A. S. P. M. A. R. J. J. A. M. A. W. and Weitz, D. A. (2013). Dna sequence analysis with droplet-based microfluidics. *Lab on a Chip*, (13):4864–4869.
- [A.S. Utada and Weitz, 2007] A.S. Utada, L.-Y. Chu, A. F.-N. D. L. C. H. and Weitz, D. (2007). Dripping, jetting, drops, and wetting: The magic of microfluidics. 32.
- [Ashkin, 1992] Ashkin, A. (1992). Forces of a single-beam gradient laser trap on a dielectric sphere in the ray optics regime. *Biophysical Journal*, 61:569–582.
- [Babak Ziaie and Siegel, 2004] Babak Ziaie, Antonio Baldia, M. L. Y. G. and Siegel, R. (2004). Hard and soft micromachining for biomems: review of techniques and examples of applications in microfluidics and drug delivery. *Advanced Drug Delivery Reviews*, 56:145–172.
- [Basu, 2013] Basu, A. S. (2013). Droplet morphometry and velocimetry (dmv): a video processing software for time-resolved, label-free tracking of droplet parameters. *Lab on a Chip*, (13):1892–1901.
- [Bewerunge and Egelhaaf, 2015] Bewerunge, J. and Egelhaaf, S. U. (2015). Experimental creation and characterization of random potential energy landscapes exploiting speckle patterns. *Physical Review A*, 93.
- [Chandrasekhar, 1943] Chandrasekhar, S. (1943). Stochastic problems in physics and astronomy.
- [Chappat, 1994] Chappat, M. (1994). Some applications of emulsions. *Colloids and Surfaces A: Physicochemical and Engineering Aspects*, 91:55–57.

- [Chaudhury and Whitesides, 1991] Chaudhury, M. K. and Whitesides, G. M. (1991). Direct measurement of interfacial interactions between semispherical lenses and flat sheets of poly(dimethylsiloxane) and their chemical derivatives. *Langmuir*, 7:1013–1025.
- [Christopher and Anna, 2007] Christopher, G. and Anna, S. (2007). Microfluidic methods for generating continuous droplet streams. *Journal of Physics D: Applied Physics*, 40:319–336.
- [Cornish, 1928] Cornish, R. J. (1928). Flow in a pipe of rectangular cross-section. *Proceedings of the Royal Society of London A*, (120):691–700.
- [Crocker and Grier, 1996] Crocker, J. C. and Grier, D. G. (1996). Methods of digital video microscopy for colloidal studies. *Colloid Interface Sci.*, 179.
- [D. Grasso and Bergendahl, 2002] D. Grasso, K. Subramaniam, M. B. K. S. and Bergendahl, J. (2002). A review of non-dlvo interactions in environmental colloidal systems. *Reviews in Environmental Science and Biotechnology*, 1:17–38.
- [Danny Van Noort and Landweber, 2004] Danny Van Noort, Z. T. and Landweber, L. F. (2004). Fully controllable microfluidics for molecular computer. *Journal of Laboratory Automation*, pages 285–290.
- [Electronics Markets Materials Division, 2009] Electronics Markets Materials Division (2009). *3M Novec 7500 Engineered Fluid*.
- [Eric K. Sackmann and Beebe, 2014] Eric K. Sackmann, A. L. F. and Beebe, D. J. (2014). The present and future role of microfluidics in biomedical research.
- [Florian Evers and Egelhaaf, 2013] Florian Evers, Christoph Zunke, R. D. L. H. J. B. I. L. A. H. and Egelhaaf, S. U. (2013). Particle dynamics in two-dimensional random-energy landscapes: Experiments and simulations. *Physical Review E*, page 022125.
- [Grier, 2003] Grier, D. G. (2003). A revolution in optical manipulation. *Nature*, 424:810–816.
- [International Commission for Uniform Methods of Sugar Analysis, 1989] International Commission for Uniform Methods of Sugar Analysis (1989). *Sucrose Solution Percent*

---

by Weight Concentration (Brix Value) Versus Refractive Index at 20 Celsius and 589nm Wavelength (per ICUMSA).

[J. Bibette et al, 1999] J. Bibette et al (1999). Emulsions: basic principles. *Reports on Progress in Physics*, 62:969.

[Jian Chen and Sun, 2012] Jian Chen, J. L. and Sun, Y. (2012). Microfluidic approaches for cancer cell detection, characterization, and separation. *Lab on a Chip*, (12):1753–1767.

[Jong-Ho Baek and Lee, 2007] Jong-Ho Baek, S.-U. H. and Lee, Y.-G. (2007). Trap stiffness in optical tweezers.

[Kwang W. Oh and Furlani, 2012] Kwang W. Oh, Kangsun Lee, B. A. and Furlani, E. P. (2012). Design of pressure-driven microfluidic networks using electric circuit analogy. *Lab on a Chip*, 12:515.

[Maqsood A. Malik and Hashim, 2010] Maqsood A. Malik, M. Y. W. and Hashim, M. A. (2010). Microemulsion method: A novel route to synthesize organic and inorganic nano-materials. *Arabian Journal of Chemistry*, pages 397–417.

[McNaught and Wilkinson, 1997] McNaught, A. D. and Wilkinson, A. (1997). Iupac compendium of chemical terminology. *Royal Society of Chemistry, Cambridge, UK*, 62(2):2188.

[Microchem Corp Newton MA, 2016] Microchem Corp Newton MA (2016). *SU-8 2000/3000 Permanent Epoxy Negative Photoresist*.

[Molloy and Padgett, 2002] Molloy, J. E. and Padgett, M. J. (2002). Lights, action: optical tweezers. *Contemporary Physics*, 43:241–258.

[Morris and Forster, 2004] Morris, C. J. and Forster, F. K. (2004). Experiments in fluids. (36):928–937.

[Olaf Wagner and Haag, 2016] Olaf Wagner, Julian Thiele, M. W. L. M. D. A. W. W. T. S. H. and Haag, R. (2016). Biocompatible fluorinated polyglycerols for droplet microfluidics as an alternative to peg-based copolymer surfactants. *Lab on a Chip*, 16:65–69.

- [Ostwald, 1896] Ostwald, W. (1896). *Lehrbuch der Allgemeinen Chemie*, volume 2. Leipzig, W. Engelmann.
- [Philipp Gruner and Baret, 2015] Philipp Gruner, Birte Riechers, L. A. C. O. Q. B. F. T. B. D. P. and Baret, J.-C. (2015). Stabilisers for water-in-fluorinated-oil dispersions: Key properties for microfluidic applications. *Current Opinion in Colloid and Interface Science*, (20):183–191.
- [Philippe Poulin and Weitz, 1997] Philippe Poulin, Holger Stark, T. C. L. and Weitz, D. A. (1997). Novel colloidal interactions in anisotropic fluids. *Science*, 275:1770–1773.
- [Piotr Garstecki and Whitesides, 2004] Piotr Garstecki, Irina Gitlin, W. D. and Whitesides, G. M. (2004). Formation of monodisperse bubbles in a microfluidic flow-focusing device. *Applied Physics Letters*, 85(13):2649–2651.
- [Rosen, 2004] Rosen, M. J. (2004). *Surfactants and interfacial phenomena*. 3 edition.
- [Rudin, 1957] Rudin, A. D. (1957). Measurement of the foam stability of beers. *Journal of The Institute of Brewing*, 63:506–509.
- [Sebastian Horstmann and Egelhaaf, 2016] Sebastian Horstmann, Jörg Bewerunge, C. Z. F. P. and Egelhaaf, S. U. (2016). Particle dynamics in rough potentials with spatial correlations.
- [Shantanu Bhattacharya and Gangopadhyay, 2005] Shantanu Bhattacharya, Arindom Datta, J. M. B. and Gangopadhyay, S. (2005). Studies on surface wettability of poly(dimethyl) siloxane (pdms) and glass under oxygen-plasma treatment and correlation with bond strength. *Journal of Microelectromechanical Systems*, 14(3):590–597.
- [Slomkowski, 2011] Slomkowski, S. (2011). Terminology of polymers and polymerization processes in dispersed systems (iupac recommendations 2011). *Pure and Applied Chemistry*, 83(12):2229–2259.
- [Sullivan and Stone, 2008] Sullivan, M. T. and Stone, H. A. (2008). The role of feedback in microfluidic flow-focusing devices. *Philosophical Transactions of the Royal Society*, (366):2131–2143.

- [Tadros, 2013] Tadros, T. F. (2013). *Emulsion Formation, Stability, and Rheology*. Wiley-VCH Verlag GmbH and Co. KGaA, 1 edition.
- [Thomas Franke and Wixforth, 2009] Thomas Franke, Adam R. Abate, D. A. W. and Wixforth, A. (2009). Surface acoustic wave (saw) directed droplet flow in microfluidics for pdms devices. *Lab on a Chip*, 9:2625–2627.
- [Töpel, 2015] Töpel, A. (2015). *Chemie und Physik der Milch*. Behr's Verlag.
- [Wang and Lee, 2013] Wang, J.-H. and Lee, G.-B. (2013). Formation of tunable, emulsion micro-droplets utilizing flow-focusing channels and a normally-closed micro-valve. *Micromachines*, 4:306–320.
- [Whitesides, 2006] Whitesides, G. M. (2006). The origins and the future of microfluidics. *Nature*, 442.
- [Xia and Whitesides, 1998] Xia, Y. and Whitesides, G. M. (1998). Soft lithography. *Annual Review of Materials Science*, 28:152–184.
- [Ying Zhang and Leong, 2013] Ying Zhang, H. F. C. and Leong, K. W. (2013). Advanced materials and processing for drug delivery: The past and the future. *Advanced Drug Delivery Review*, (65):104–120.
- [Yung-Chieh Tan and Lee, 2008] Yung-Chieh Tan, Y. L. H. and Lee, A. P. (2008). Microfluidic sorting of droplets by size. *Microfluidics and Nanofluidics*, 4:343–348.
- [Zhu and Nguyen, 2010] Zhu, G. and Nguyen, N.-T. (2010). Particle sorting in microfluidic systems. *Micro and Nanosystems*, 2.



# Ehrenwörtliche Erklärung

Hiermit versichere ich, die vorliegende Masterarbeit selbstständig verfasst und keine anderen als die angegebenen Quellen und Hilfsmittel benutzt zu haben. Alle Stellen, die aus den Quellen entnommen wurden, sind als solche kenntlich gemacht worden. Diese Arbeit hat in gleicher oder ähnlicher Form noch keiner Prüfungsbehörde vorgelegen.

Düsseldorf, 25. September 2017

Sebastian Horstmann